Excitonic couplings and interband energy transfer in a double-wall molecular aggregate imaged by coherent two-dimensional electronic spectroscopy

F. Milota,[1] J. Sperling,[1] A. Nemeth,[1] D. Abramavicius,[2] S. Mukamel,[2] and H. F. Kauffmann[1,3,a]

[1]*Department of Physical Chemistry, University of Vienna, Währingerstraße 42, A-1090 Vienna, Austria*
[2]*Department of Chemistry, University of California, Irvine, California 92697-2025, USA*
[3]*Ultrafast Dynamics Group, Faculty of Physics, Vienna University of Technology, Wiedner Hauptstrasse 8-10, A-1040 Vienna, Austria*

The early stage of molecular excitonics and its quantum-kinetic dynamics in the multiband, bitubular cyanine dye aggregate C_8O_3 at room temperature are revealed by employing two-dimensional (2D) coherent electronic spectroscopy in the visible spectral region. The sub-20 fs measurements provide a direct look into the details of elementary electronic couplings by spreading spectroscopic transitions into two frequency axes. Correlation spectra of rephasing ($k_I = -k_1 + k_2 + k_3$) and nonrephasing ($k_{II} = +k_1 - k_2 + k_3$) data in emission ($\omega_3$)-absorption ($\omega_1$) 2D-frequency space image interband excitons into cross-peak signals and unveil the quantum-dissipative regime of exciton relaxation. Spectral streaking of cross peaks directly reveals interband dephasing and exciton population relaxation on the road to tube-to-tube energy transfer without making recourse to an *a priori* model. Theory and simulations, based on an effective multilevel scheme and a quantum-dissipative model with experimental pulse envelopes, explain the origin of the cross peaks, reveal the underlying sequences of electronic transitions, recover the streaking patterns of relaxing cross peaks along ω_1, and reconstruct the space-energy pathways of electronic excitation flow. © 2009 American Institute of Physics. [DOI: 10.1063/1.3197852]

I. INTRODUCTION

One of the challenges in supramolecular chemistry and molecular nanoengineering is the identification of distinct molecular features and functions that are derived from naturally occurring biomacromolecular systems and using these properties in biomimeting technical applications. For example, to imitate the optimized energy flow in the biological light harvesting pigment complex by tailor-made, artificial molecular ensembles. Such molecular architectures, devised to mimic migrational energy trapping and charge separation, must constitute photoantennae, storage rings, and a nonstatistical energy gradient, where the photon absorbed is guided without substantial losses as a molecular exciton on a selective, highly directional space-energy pathway to the exit channel of chemical conversion.[1,2]

One appealing synthetic route is the potential of certain dye molecules to self-assemble in concentrated solutions to quasi-one-dimensional (1D) aggregates.[3,4] Upon optical excitation, the (weakly disordered) site arrangement with their site transition dipoles in close spatial proximity gives rise to Frenkel-type excitons[5] that are shared by many molecules. *J*-aggregates are the closest molecular analog of an inorganic semiconductor; their unique excitonic structure and high energy transfer efficiency are relevant to many applications such as artificial photosynthesis, polariton science, and sensitized chemical dynamics.[6] The line shape of the redshifted (single) *J*-band in linear aggregates reflects interesting cooperative spectroscopic properties such as collective in-phase absorption, coherent super-radiant emission, electronic coupling, and exchange narrowing, which have received both continuous theoretical[7–10] and experimental[11,12] interest. In particular, at low phonon temperatures and predominant static site disorder, the Frenkel exciton picture has been successful in explaining the linear absorption (LA), fluorescence, and excited-state absorption (ESA) in pump-probe (PP) spectra.[13]

Breakthroughs in molecular self-assembly[14] and nanochemical engineering[15] have paved the way for tailor-made organic dye chromophores with supramolecular structures and special functionality. Common aggregate forming cyanine dyes can be designed by controlled chemical linking to hydrophilic and hydrophobic sidechains/substituents to exhibit amphiphilic properties.[16] This interaction of hydrophilic/hydrophobic forces in combination with intermolecular forces and entropy minimization leads to self-assembly into a double-walled tubular array as a new structural motif.[17] Carbocyanine-type tubular aggregates are therefore very promising candidates for artificial light harvesters and electronic energy transport systems.[18] Their architecture is similar to the rod elements in light-harvesting chlorosomes of green photosynthetic bacteria and plants where thousands of bacteriochlorophyll (BChl) molecules self-assemble to a rod-shaped supramolecular antenna system.[19,20] In particular, for the chiral chlorosomes of *Chlo-*

a)Electronic mail: harald.f.kauffmann@univie.ac.at.

roflexus aurantiacus and *Chlorobium tepidum* a detailed model for the spatial organization of the BChl molecules in the rods has been proposed on the basis of various spectroscopic techniques and molecular modeling.[21] Femtosecond four-wave-mixing (FWM) techniques, such as three-pulse photon-echo spectroscopy with homodyne detection, in conjunction with theoretical treatments[9,22–24] have led to progressively deeper understanding of the microscopic dynamics of aggregates for some time past.[11,25–27] These excitation-probing configurations measure time-integrated and phase-averaged signal-intensities ($|P^{(3)}(t_1,t_2,t_3)|^2$); they interrogate the loss of the squared polarization by 1D projections on distinct delay-times t_i. While exciton dynamics and relaxation in population space can be verified with little difficulty almost routinely, it is hard to extract information about the nature of electronic and nuclear couplings, which are the underpinnings of spatial optical femtosecond dynamics from conventional FWM experiments.

Recently, heterodyne-detected two-dimensional coherent electronic spectroscopy (2D-ES) that relies on coherent, phase-locked three-pulse excitations and measures the time- and phase-resolved field amplitude $E_s^{(3)}(t_1,t_2,t_3,\phi) \propto -iP^{(3)} \times (t_1,t_2,t_3,\phi)$ in terms of its double Fourier transform (FT) $E_s^{(3)}(\omega_1,t_2,\omega_3,\phi)$ has emerged as the cutting-edge technique for probing femtosecond molecular correlations in real time.[28–31] 2D-ES experiments, culminating so far on the biological, light harvesting Fenna-Matthews-Olson (FMO) complex, have revealed exciton couplings, space-energy excitation flow,[32] cross-peak specific polarization shaping,[33] and coherent optical dynamics.[34]

We report the 2D-ES of a tubular, synthetic aggregate. We measure the first steps of molecular excitonics in the double-wall aggregate C_8O_3.[35] Our combined experimental/theoretical study is intended to explicate the early signatures of exciton interband couplings and to trace the dynamic motifs of its quantum dissipation that set the preliminaries for tube-to-tube energy transfer. In Sec. II, the linear spectroscopic features and the bitubular architecture of C_8O_3 are recapitulated with regard to the forthcoming 2D-ES experiments (Sec. IV). Section III describes the principles of coherent 2D-ES based on signal-field heterodyning and double Fourier transform. Further, it outlines a typical protocol of a 2D-ES experiment and describes details of sample preparation. In Sec. IV experimental 2D correlation and relaxation spectra of C_8O_3 in water are presented, followed by the decomposition of the absorptive 2D-ES signal part into rephasing (k_I) and nonrephasing (k_{II}) contributions in Sec. V. The simulation procedure is outlined in Sec. VI. The discussion of the experimental and theoretical results is given in Sec. VII. The summary and concluding remarks are contained in Sec. VIII.

II. ABSORPTION (1D) SPECTROSCOPY BANDS, TUBES, AND ELECTRONIC COUPLINGS

The bitubular architecture of the amphiphilic C_8O_3 aggregate in water is a striking example for the power of self-association to build up nanoscaled molecular assemblies with supramolecular architecture. Selective hydrophobic and hy-

drophilic interactions among the monomers promote the formation of double-walled structures, consisting of two tubes with diameters of 10 nm (inner tube), respectively 14 nm (outer tube). The distance between the inner and the outer tube is a few nanometers (≈ 4 nm) while the length of the two tubes ranges from several hundreds of nanometers to tens of micrometers. In the final stabilization process, the double-walled strands further build up a helical organization in which up to five tubules twist around each other [Fig. 1(a)], forming a chiral supramolecular structure.[36] The C_8O_3 system may be considered, therefore, as a molecular analog to a double-wall carbon nanotube, where small changes in the cylinder lengths and in the few nanometer wall-to-wall distances due to altering molecular orientations substantially determine the helicity and the details of the band structure. As a consequence, the number of electronic transitions in the bitubular aggregate is first controlled by stereochemical factors. In the absence of disorder, i.e., assuming lattice periodicity, the exciton bands corresponding to the inner (1) and outer (2) tubes are described by Bloch-type k-space wave functions.[37] Owing to its cylindrical symmetry, this implies splitting of the absorption dipole into two longitudinal $\parallel_1$, $\parallel_2$ (parallel to the cylinder axis) and two energy-degenerate transversal transitions $\perp_1$, $\perp_2$ perpendicular to the cylinder axis for each tube 1 and 2 [Fig. 1(b)], with the frequency difference being inversely proportional to the tube diameter $\Delta\omega_{1,2} \propto d_{1,2}^{-1}$.

It is hard to quantify the electronic couplings of the outer tube 2 to the inner tube 1.[38] In the absence of electronic tube-to-tube interaction, the line spectrum of the longitudinal electronic transition $\parallel_2$ of the outer tube 2 (with a larger diameter d_2 and higher energy of $\perp_2$) will shift to the blue. However, the frequency splitting between $\parallel_2$ and its orthogonal transversal ones $\perp_2$ will become smaller according to $\Delta\omega_2 \propto d_2^{-1}$, resulting in degeneracy of the perpendicular bands $\perp_1$ and $\perp_2$ [cf. Fig. 1(b)].

The splitting pattern in Fig. 1(b) is broadened due to excitonic intraband disorder and dynamic reservoir fluctuations from the solvent. This naturally raises the question to which extent these individual splittings survive the mixing of exciton bands,[39] apart from the effects caused by electronic interband couplings that are still ruled out for the present. The absorption spectrum of C_8O_3 in water [Fig. 1(c)] shows both bands I and II broadened with widths due to static and dynamic site fluctuations smaller than the energy difference between dipoles I and II and with full width at half maximum broadenings $\Gamma_I < \Gamma_{II}$ and different electronic dipole intensities. Polarized light measurements identify the transitions I and II as highly polarized parallel to the long cylinder axes for tubes 1 and 2, respectively, with center positions of 16 670 and 17 170 cm^{-1}.[40] As a consequence of disorder, the two orthogonal transitions $\perp_1$ and $\perp_2$ merge into one band III which further overlaps with band II. It only shows up as a weak shoulder at 17 380 cm^{-1} and is subject to excitations predominantly perpendicular to the long axis in tubes 1 and 2. Each of these excitonic subensembles corresponding to band transitions I, II, and III is expected to contain several hundred to thousand monomer units with slightly varying band disorder σ from weak (I) to moderate (II, III) and with
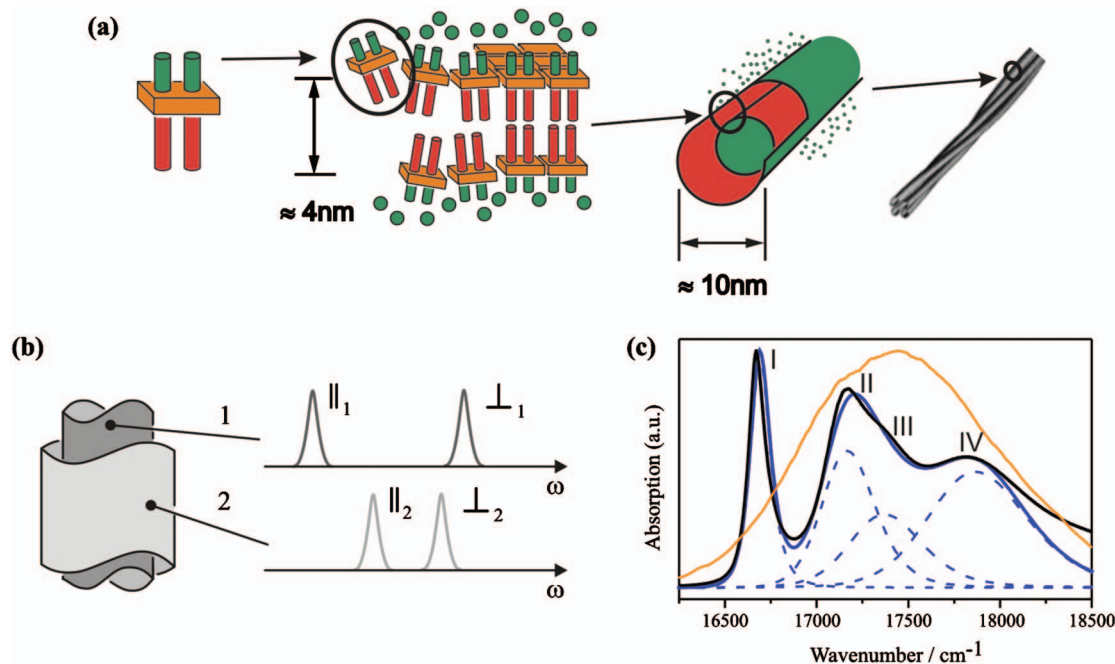
FIG. 1. (a) Cartoon sketching the self-assembling of C_8O_3 monomers into an array of molecular nanotubes: Dye molecules (chromophore: Orange) with hydrophobic (red) and hydrophilic (green) substituents zip into double-wall cylindrical motifs and helical suprastructures in aqueous solution (cryo-transmission electron microscopy image taken from Ref. 17). (b) The structure of C_8O_3 consists of two tubular aggregates constituting of an inner (1) and an outer cylinder (2). Both cylinders contribute one parallel ($\parallel_1, \parallel_2$) and two energy-degenerate perpendicular transitions ($\perp_1, \perp_2$) to the LA spectrum. Due to the different diameters of the two cylinders, the frequency splittings between these two components are different. (c) The experimental LA spectrum of C_8O_3 (black) in aqueous solution with parallel polarized bands I and II peaking at 16 670 and 17 170 cm^{-1}, respectively. Band III (17 380 cm^{-1}) is a shoulder indicating the degenerate and inhomogeneously eroded transversal transitions $\perp_1, \perp_2$. The experimental spectrum can be satisfactorily described by four electronic oscillators (blue dashed lines represent their individual contributions; blue solid line shows their sum). Band IV is related to an ensemble of weaker, less collective dipoles being the signature of the supermolecular helical regime. The pulse envelope is shown as orange line.

intraband excitonic couplings V, each V_j exceeding its inhomogeneous band broadening ($V_j/\sigma_j > 1$). Finally, C_8O_3 shows an additional high-energy band dipole IV at 17 860 cm^{-1} with low intensity and larger bandwidth. Band IV may be assigned to electronic excitations delocalized across several closely lying tubules in the helical regime of twisted double-wall strands, similar to the collective high-energy excitations in chlorosomal stacks.[41]

The experimental LA spectrum of C_8O_3 [black solid line in Fig. 1(c)] can be reconstructed satisfactorily by four electronic oscillators (blue dashed lines) with static site disorder and dynamic fluctuations. Clearly, information about interband and tube-to-tube electronic couplings, energy transfer mechanism, or its time scales cannot be extracted from the highly congested linear spectrum. Simulations in a finite-sized, chain-to-chain geometry of two closely spaced linear chains, mimicking tube-to-tube electronic interaction in the absence of the supramolecular structure, show wave-function delocalization and excitonic interband, non-Förster-type transfer between the chains described by phonon-induced population relaxation.[39] Time-resolved streak-camera fluorescence and spectrally resolved PP experiments on C_8O_3 and related aggregates suggest that these arrays are proto-typical band-to-band energy transfer systems[40,42] of relaxing excitations in population space. The elementary couplings prior to the birth of population are, therefore, inferred only indirectly by these studies. Homodyne detected signals that measure $|P^{(3)}|^2$ do not directly reveal the couplings. Since

phase memory of initial band-to-band coherence is averaged out by time-integrated homodyne detection, neither electronic delocalization and band-to-band mixing nor the early quantum dissipation is resolvable even by employing time-resolved gating[43] or spectrally dispersed FWM (Ref. 44) experiments.

Based on recent advances,[29,32,45] it is clear that hetero-dyne detection of the field $E_s^{(3)}$ and its double Fourier transform is the instrumentation of choice in the study of molecular femtosecond couplings. By employing coherent 2D-ES, we demonstrate measurements of off-diagonal peaks in frequency-frequency correlation plots and thus directly probe electronic coupling and electron-phonon scattering. The latter elementary processes are the underpinnings of exciton dynamics allowing the entire state-to-state energy transfer pathways of optical interband transport in C_8O_3 to be imaged in real time.

III. EXPERIMENTAL DETAILS

A. Time- and phase-resolved coherent 2D-ES

Early theoretical work and analysis of the control of higher-order, nonlinear molecular field amplitudes in phase-sensitive optical spectroscopy[46] stimulated the technological advance of time- and phase-resolved 2D FWM techniques. Although two-dimensional infrared spectroscopy[47] and 2D-ES (Ref. 48) have been established for nearly one decade, the technical realization of 2D-ES in the visible part of
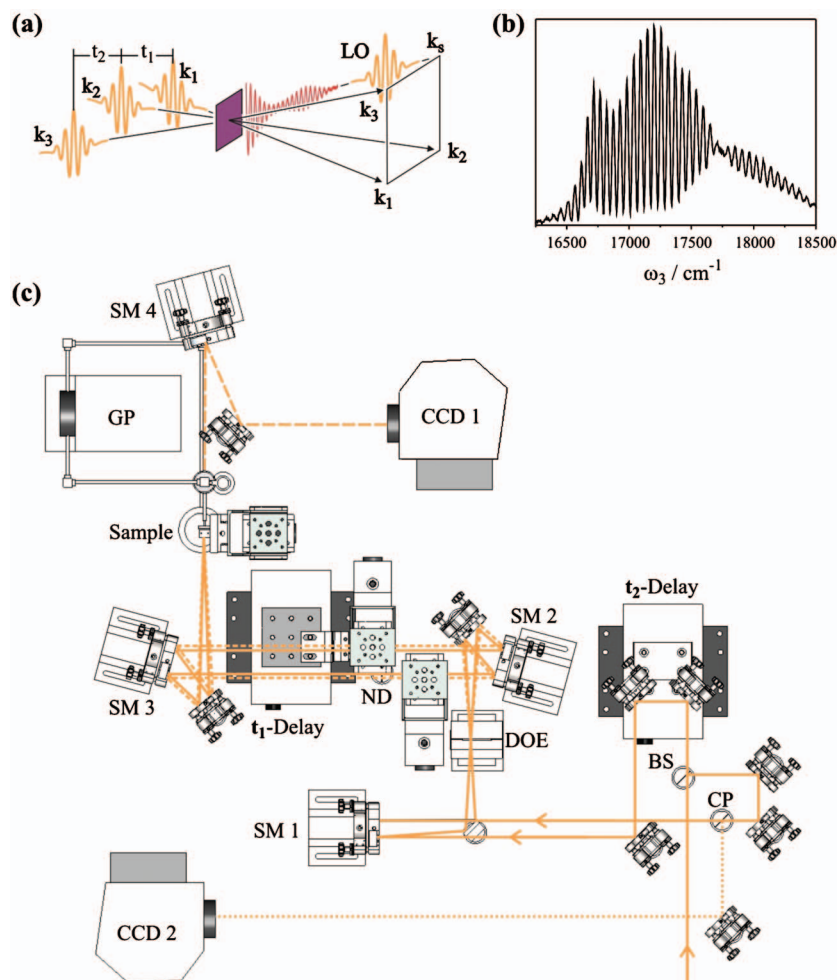
FIG. 2. (a) Definition of time delays and boxcar geometry in the coherent 2D electronic spectroscopy experiment. The diffracted k_s propagates into the same direction as the LO. The nonlinear signal is subjected to spectral interference with the preceding LO for signal reconstruction in ω_3 frequency domain. (b) A typical spectral interferogram for t_1 and t_2 set to zero. (c) The NOPA output is split into two beams at a beam splitter and one is given a variable delay. The two beams are focused by a spherical mirror (SM 1) onto a diffractive optics element (DOE), which is optimized to diffract 30% of the intensity of each beam into the $\pm$ first diffraction orders (upward diffracted beams are indicated by the solid line, downward diffracted beams by the dashed line). The four beams resulting from the DOE are parallelized by a spherical mirror (SM 2) and are located at the corners of a square forming a "boxcar" pattern. The two pump beams (k_1, k_2) are separated by the coherence time t_1 by means of a pair of moveable glass wedges in beam 2 (t_1-delay). k_2 and k_3 are delayed by time t_2 by a conventional delay stage before the DOE (t_2-delay). The fourth beam in the boxcar pattern is the weak reference pulse k_{LO}. It is attenuated by a neutral density (ND) filter and passes through the sample preceding the excitation pulses (k_1, k_2, k_3) by ≈ 550 fs. After passing the sample it propagates collinearly with the signal field. Heterodyne detection with the LO pulse in a CCD spectrometer (CCD 1) is implemented to completely characterize the signal electric field (spectral interferometry). A second CCD camera (CCD 2) serves to reduce noise in separately recorded spectrally resolved PP spectra.

the spectrum is a more recent breakthrough. This has been due to the difficulties with the necessary phase stabilization of the signal fields and their precise experimental Fourier transform. These difficulties have finally been solved by the progress in diffractive optics pulse phase locking,[45,49] spectral interferometry,[50,51] and improvement in delay-time precision by two orders of magnitude.[45,52]

In coherent 2D-ES, the fundamental quantity of interest is the time-dependent, oscillatory molecular signal field $E_s^{(3)}$ $\times (t_1, t_2, t_3)$, where t_1 and t_2 represent the two time intervals between the three pulse-molecule interactions and t_3 denotes the time elapsed after the third pulse and the onset of the signal field [Fig. 2(a)]. Under perfect phase matching, the diffracted field is proportional to the third order polarization $P^{(3)}(t_1, t_2, t_3)$ with signal wave-vector architecture $k_I = -k_1 + k_2 + k_3$ [photon echo (PE), rephasing]

$$P^{(3)}(k_I, t_1, t_2, t_3) = \int dt_3 \int dt_2 \int dt_1 R^{(3)}(t_1, t_2, t_3) E_3(k_3, t - t_3)$$
$$\times E_2(k_2, t - t_3 - t_2) E_1^*(k_1, t - t_3 - t_2 - t_1) \quad (1)$$

and is expressed as a convolution of the optical response function $R^{(3)}(t_1, t_2, t_3)$ and the electric fields $E_1(k_1, t)$, $E_2(k_2, t)$, and $E_3(k_3, t)$ of the laser pulses with wave-vectors k_1, k_2, and k_3, respectively. $k_{II} = k_1 - k_2 + k_3$ (optical free induction decay, nonrephasing) can be calculated similarly. Expressions of 2D nonlinear signals referring to these experiments are given in Sec. VI and the Appendix. The first pulse (k_1) creates a coherence between the ground and the excited electronic state. The second pulse (k_2 after time t_1) converts the freely evolving coherence into an electronic population (population grating) and/or a vibrational coherence in the ground or excited state which relaxes via T_1 processes for a

time t_2. Finally, the third pulse (k_3 after time t_2) interacts with the decaying population/coherence and creates a coherent macroscopic dipole whose super-radiance generates the signal along k_I or k_{II}, depending on the order of the interactions. Feynman graphs, depicting Liouville-space density matrix pathways of off-diagonal coherences and diagonal populations, provide a pictorial representation of rephasing and nonrephasing signals (Sec. V) and are indispensable in the analysis of the signals.[53] The graphs can be expanded to include relaxational pathways and describe exciton population transfer and related dephasing processes (Sec. IV).

B. Coherent 2D electronic spectrometer

Our laser configuration is a solid state laser (Verdi V18, Coherent, Inc.) pumped Ti:sapphire regenerative amplifier system (Rega 9050, Coherent, Inc.) in conjunction with a noncollinear optical parametric amplifier (NOPA) (Ref. 54) operating at a repetition rate of 200 kHz. This configuration yields tunable sub-20 fs pulses with pulse energies of several hundred nanojoules in the visible (470–720 nm) and is complemented by a zero-additional-phase (ZAP) spectral phase interferometry for direct electric field reconstruction (SPIDER) (Ref. 55) that characterizes the excitation pulses in a noninvasive fashion. This combination of noncollinear frequency conversion and high repetition rate ensures short accumulation times, high temporal resolution, and 2D spectra with very good signal to noise ratios.

In our setup [Fig. 2(c)], generation of phase-locked excitation pulses, detection of time-resolved, phase-sensitive signals, and their translation into frequency-frequency space of the double Fourier transform signal field follow the experimental configuration given in Refs. 45, 56, and 57. The 16 fs excitation pulses (center wavelength of 17 500 cm^{-1}) are passively phase locked by the implementation of a diffractive optics based interferometer[45] that minimizes the phase drift between the two pairs of pulses, i.e., pulses 1, 2 and pulses 3, LO (local oscillator). Each pair (1, 2 and 3, LO) is derived from the $\pm$ first diffractive order components of a laser pulse incident on a transmission grating (125 lines/mm), each one with constant relative phase ($\phi_1 - \phi_2$), ($\phi_3 - \phi_{LO}$) for varying delay times, to give a boxcar pattern, which is then imaged onto the sample [cf. Fig. 2(a)]. The t_1 delay is scanned with high interferometric precision (0.66 fs step size) by using a movable pair of glass wedges[52] inserted into the path of k_2, which are mounted on a motorized linear translation stage. Translating one wedge with respect to the other in the pair affects the optical path length of the pulse, thereby varying the arrival time at the sample with a delay precision of 5.3 as. This enables the correct measurement of the echo-signal $E_s^{(3)}(k_s, t_1, t_2, t_3)$ without undersampling, i.e., probing both the center frequency of the optical cycle and the damping from the overall frequency dynamics of the relaxing signal field in an unbiased fashion. To balance the dispersion for all three excitation pulses, identical static glass wedge pairs are inserted into the paths of k_1 and k_3.

Frequency-frequency 2D spectral amplitudes and the absorption/dispersion spectra are obtained by heterodyning the signal field $E_s^{(3)}(k_s, t_1, t_2, t_3) \propto P^{(3)}(k_s, t_1, t_2, t_3)$ with the

LO pulse E_{LO} (pulse 4) and spectral interferometry via Fourier inversion steps.[29,50] The LO and the signal field, propagating collinear after the sample with E_{LO} preceding the other pulses by $\sim$550 fs, are sent into a spectrometer and dispersed with a 1800 mm^{-1} grating on a charge coupled device (CCD) array detector. A typical spectral interferogram for $t_1 = t_2 = 0$ is shown in Fig. 2(b). Neglecting rising edge convolution effects in the optical response field due to the finite excitation pulses, the squared heterodyned signal intensity in frequency space, Fourier inverted with respect to t_3 at a distinct t_1 and t_2, is

$$I_{het}(t_1, t_2, \omega_3) = |E_{LO}(\omega_{LO})|^2 + |E_s(\omega_3)|^2$$
$$+ E_{LO}(\omega_{LO})E_s(\omega_3)\cos(\phi_{LO} - \phi_s + \omega_3 t_{LO}), \quad (2)$$

where ϕ_{LO} and ϕ_s are the spectral phases of the LO E_{LO} and the signal field E_s, respectively, and $\omega_3 t_{LO}$ denotes the relative phase between pulses k_3 and LO k_{LO} at delay time t_{LO}. Further Fourier transform/filtering procedures and ZAP-SPIDER local field characterization enable to eliminate the LO $E_{LO}(\omega_{LO})$-term from the cross term. Numerical Fourier transform with respect to t_1 scanning from maximum negative delay to maximum positive delay yields the desired second frequency axis ω_1 of the signal in the complete amplitude/phase representation of the molecular electric field. For the absorptive/imaginary parts of the 2D spectra, determination of the absolute signal phase is necessary by comparison with a frequency resolved PP signal. Shifting the projection of the real part of $E_s^{(3)}(\omega_1, t_2, \omega_3)$ into an overlay representation with the PP spectrum (a procedure termed *phasing*) yields the absolute spectral phase from the unknown off-set of the spectral interferometer.[29,51,58] The absorptive part can be interpreted as the transient field amplitude at a particular probe frequency ω_3, induced by a specific excitation frequency ω_1.

With regard to the interpretation of experimental exciton signatures, we note in the forefield of the experimental results (Sec. IV) that the negative time delay corresponds to the reversal of the interaction sequence of pulses k_1 and k_2. Since the signal is measured in the direction $-k_1 + k_2 + k_3$, at positive delay times, the $k_I = -k_1 + k_2 + k_3$ (rephasing) signal is detected, whereas at negative delay times the $k_{II} = +k_1 - k_2 + k_3$ (nonrephasing) signal is detected.[59] The full Fourier transform (including both the positive and the negative delays) can thus be decomposed as

$$E_{abs}^{(3)}(\omega_1, t_2, \omega_3) = E_{k_I}^{(3)}(\omega_1, t_2, \omega_3) + E_{k_{II}}^{(3)}(\omega_1, t_2, \omega_3). \quad (3)$$

Because of the difference in the sign of the phase accumulated during the coherence periods t_1 and t_3, a strong, collective signal is observed along the diagonal frequency axis ($|\omega_1| = \omega_3$) for the rephasing signal k_I. In contrast, the nonrephasing[59] k_{II} signal spectrum is oriented along the antidiagonal axis.[59,60] The superposition of k_I and k_{II} in the measuring process determines the shape of the experimental diagonal and off-diagonal correlation peaks in Sec. IV.
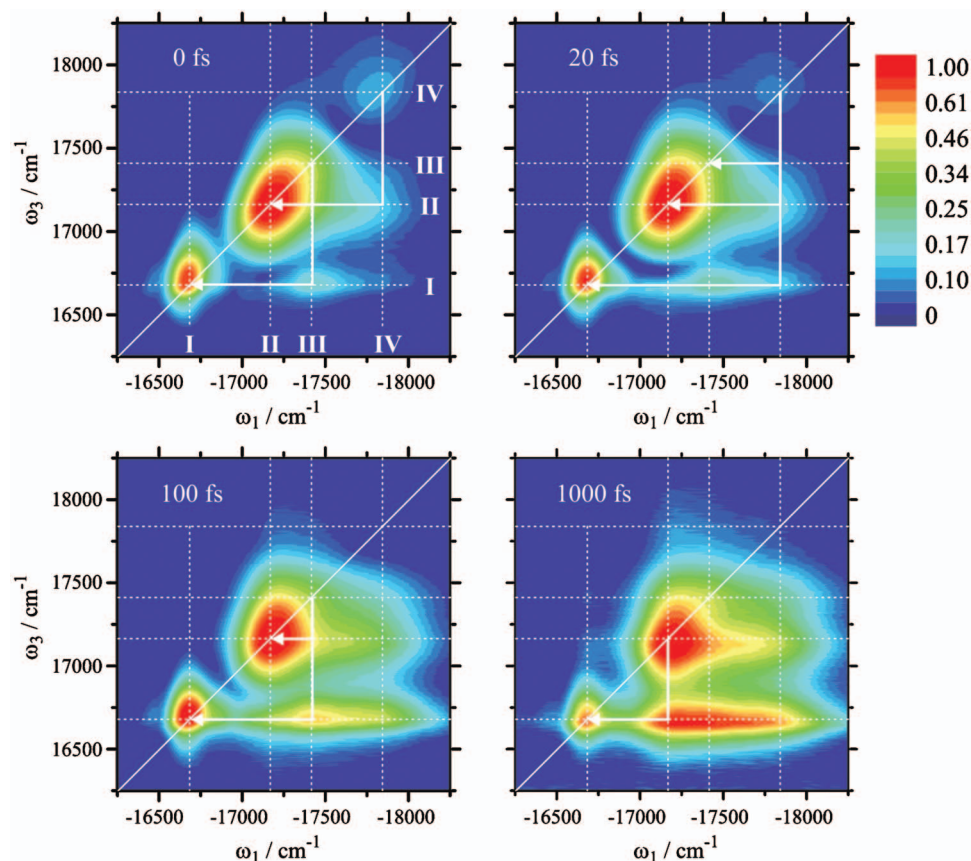
FIG. 3. 2D amplitude frequency-frequency correlation and relaxation spectra of C_8O_3 in water for t_2-times of 0, 20, 100, and 1000 fs. All spectra are normalized to their respective maximum absolute value; color scale is based on a arcsinh-weighting function starting at $\sim$5% of signal intensity. Diagonal correlation peaks I, II, III (shoulder), and IV correspond to the 1D LA peaks. The existence of cross peaks is paradigmatic for electronic interband correlations and indicates strong coupling between bands III/I and IV/II as well as weaker couplings among bands IV/I and II/I, respectively. White arrows indicate the roads of excitonic energy transfer nourished by the interplay of weak to moderate interband couplings and band-to-band population relaxation.

C. Sample preparation and handling

The carbocyanine dye C_8O_3 was purchased from FEW Chemicals (Wolfen, Germany) and has been used as received. The aggregate solution has been prepared according to literature.[61] The dye concentration in aqueous solution is 1×10^{-4} mol/l. To eliminate signals from cuvette windows (which can be of the same magnitude as the third order signals), we have implemented a gravity driven, wire-guided drop jet[62,63] for the circulation of the sample. Note that measuring in the jet avoids the otherwise necessary measurement and compensation of the sample cell windows prior to experiment by readjusting the fused-silica prism compressor. On the other hand, the flow in the jet and the shear force lead to partial orientation of the aggregate chains along the flow direction, as observable in linear dichroism spectra.[64] Note that since the excitation beams are polarized perpendicular to the flow, we should preferentially excite the transversal transitions and merely to a minor extent the longitudinal ones. Finally, to avoid undesired higher-order effects, such as exciton-exciton annihilation and nonresonant signals from the solvent, excitation beams are attenuated to yield not more than 3 nJ of energy in each of the excitation pulses. With a beam diameter of 5 mm at the focusing mirror (SM 3 in Fig. 2), this corresponds to a fluence of 3.6×10^{14} photons/cm^2, leading to the excitation of 1.7% of the molecules in the focal volume. This excitation density has been shown to be low enough to exclude annihilation effects from contributing to the detected signals.[40]

IV. EXPERIMENTAL RESULTS——PEAKS AND STREAKS OF EXCITON DYNAMICS

The bandwidth of our 16 fs pulses ($\sim$1000 cm^{-1}) is broad enough [orange solid line in Fig. 1(c)] to entirely cover the C_8O_3 aggregate bands when tuned by the NOPA to a center frequency of 17 500 cm^{-1}. Upon resonant excitation, the pulse creates a polarization that includes in-phase coherent preparation of four excitonic transition dipoles I, II, III, and IV, respectively. The entire tube system (with single- and double-exciton band structure) can then be considered either as an ensemble of four, noninteracting three-level systems in the absence of band-to-band coupling, or as an array of correlated interband excitations in the delocalized eigenstate representation if electronic coupling is present (cf. Sec. VI).

A. Amplitude correlation ($t_2 = 0$ fs) and relaxation spectra ($t_2 > 0$ fs)

Figure 3 shows the amplitude of the complex 2D correlation spectrum of C_8O_3 containing the sum of the absorptive (real) part and the dispersive (imaginary) part $E^{(3)} \times (\omega_1, t_2, \omega_3) = \sqrt{(E_{abs}^{(3)})^2 + (iE_{disp}^{(3)})^2}$ as a function of the conjugate variables ω_1 and ω_3 recorded at t_2 delays of 0, 20, 100, and 1000 fs. In the correlation spectrum ($t_2 = 0$ fs) bands I–IV appear as 2D peaks along the main diagonal ($|\omega_1| = \omega_3$) and reflect the LA by projection along the ω_3-axis. As in LA band III is not fully resolved. The relative intensities of the diagonal peaks are different from the absorption spectrum, since they scale as $|\mu_i|^4$ with the transition dipole rather than $|\mu_i|^2$ as in LA. In addition, the pulse power spectrum,

optimized to cover the entire region of transitions, gives rise to different center-frequency detunings for each of the band transitions and thus affects the relative excitation intensities of the bands. Overall, peak IV is therefore less intense in the 2D spectrum than in 1D LA.

Both diagonal peaks of bands I and II are substantially rotated off of the main diagonal into the $|\omega_1| > \omega_3$ regime indicating a strong contribution of ESA into their two-exciton bands. Contrarily, the intercylinder band transition IV behave quite normal. Its intensity is weak and its spectral contour shows weak ellipticity only with its longer axis symmetrically oriented along the main diagonal. It appears to be affected substantially by a density of states (DOS) of disordered and weakly collective (monomeric) absorbers which mix with the wave functions of the collective, in-phase transitions into the excitonic band-structures I, II, and III, respectively. Band-symmetry breaking in peak IV together with its extremely short survival time due to dynamic fluctuations have tremendous impact on the pattern formation of energy flow in C_8O_3 and the details of its overall optical dynamics (Sec. VII).

The observation of cross peaks of varying intensities in the off-diagonal $|\omega_1| > \omega_3$ regime at $t_2 = 0$ fs is a very striking result. The origin of these signals—not detectable by linear or 1D nonlinear spectroscopies—is symptomatic of electronic band-to-band coupling and indicates quantum-mechanical interband combination transitions of spatially correlated transition dipoles sensing one another's presence by common ground states.[65,66] The predominant cross peaks result from correlations between bands IV and II and III and I. Further, a lower intensity cross peak is indicative of weak coupling between IV and I and II and I.

The correlation spectrum is strongly asymmetric and favors cross peaks in the low-energy ($|\omega_1| > \omega_3$) triangle. This is accompanied by the untypical spectral orientations of the off-diagonal peaks, which are closely related to the asymmetry of the correlation matrix. They are no longer parallel to the main diagonal as expected for a positive motional correlation at $t_2 = 0$ fs,[67] but rather horizontally aligned, i.e., spectrally elongated parallel to the ω_1-axis. This tendency toward early relaxation of cross peaks is mainly caused by the finite width of the excitation pulses and uncorrelated fluctuations of the exciton bands. Since the experimental 2D data are sub-20 fs pulse convolutions (and not corrected by numerical inversion), the finite time shift implies a systematic uncertainty in the delay times and falsifies, in particular, the k_2/k_3 overlap region at $t_2 = 0$ fs. Due to the finite pulse duration, the initial phase of interband quantum interference gets perturbed by dynamic fluctuations. Consequently, interband dephasing and electron-phonon coupling direct uncorrelated populations, preferentially into the low-energy interband states, which when being probed by the interrogating k_3 pulse promote increasing cross-peak intensities predominantly in the $|\omega_1| > \omega_3$ regime. Fast coherence loss thus breaks the symmetry of the excitation correlation matrix where the spectral contour of the cross peaks rotates from an alignment originally parallel to the main diagonal into an orientation parallel to the ω_1-axis. This spectral change goes hand in hand with the growth of the antidiagonal width

which reflects homogeneous electron-phonon coupling and also affects the formation of the early horizontal streak.

Cross signals at $t_2 = 0$ fs are in our experiments generally weakly relaxing interband coherences with a more or less considerable loss of phase memory. Because of the warm phonon environment of the room temperature experiments and the strong irreversibility of interband transfer triggered by the high-energy peak IV, dissipative excitons at the doorway of population transfer are a realistic terminology in this stage of quantum-kinetic relaxation. Increasing the waiting-time t_2 promotes the production of (tail-state) populations which energetically spread along the main diagonal trace and change frequency space via spectral diffusion.[68] Consequently, the interrogating third pulse with varying waiting-time t_2 senses increasing populations which cause the cross-peak signals both to grow in intensity and spectrally streak along ω_1 via stimulated emission (SE') and ESA' (cf. below). Note that the bulging signal of overlapping II and III diagonal peaks is indicative of III/II coupling, but it remains overall concealed in the presentation of the amplitude spectrum. Since the 2D amplitude spectrum combines both the absorptive and the dispersive part of the 2D Fourier transform, information about the sequence of optical processes and intermolecular details is limited. Independent inspection and evaluation of absorptive spectra [Fig. 5] help to disentangle the details of optical processes concealed in the amplitude spectra. Thus, they allow to dissect and extrapolate the various interferences inherent to the cross peaks and furthermore, for varying t_2-times, to track their quantum-dissipative pathways that form up the observed experimental 2D patterns.

B. Absorptive part correlation spectrum ($t_2 = 0$ fs)

As an introduction to the forthcoming 2D absorptive part spectra and their descriptive interpretation, we briefly consider the underlying processes that may contribute to FWM signals in a typical band-to-band interaction scheme.[30] As the 2D data in Fig. 3 show a substantial admixture of couplings, a delocalized five-level scheme in the eigenstate basis [Fig. 4(a)], modeling a pair of excitonic band dipoles (e.g., the III and I interactions), is closer at hand than the (equivalent) local site basis set to track the optical pathways of both independent and correlated (combination) transitions.

The labels of the scheme in Fig. 4(a) represent the relevant manifolds of states, g-ground state, e-single exciton states, and f-double-exciton states, and arrows indicate resonant optical transitions. This scheme allows for tracking the entire optical pathways from both independent and correlated transitions. In Fig. 4(b) the Feynman diagrams for the level scheme in Fig. 4(a) feature the rephasing part, i.e., the rotating wave approximation (RWA) photon-echo signals in terms of time-ordered, resonant transition sequences and their Liouville-space pathways. Four interaction events (wavy line arrows) happen chronologically from bottom up, while two vertical lines denoting $|ket\rangle$ and $\langle bra|$ show the free evolution of the density matrix state in each interval between interactions.[53] The first interaction causes the system's density matrix into a one-exciton coherence (ρ_{ge}). After interac-
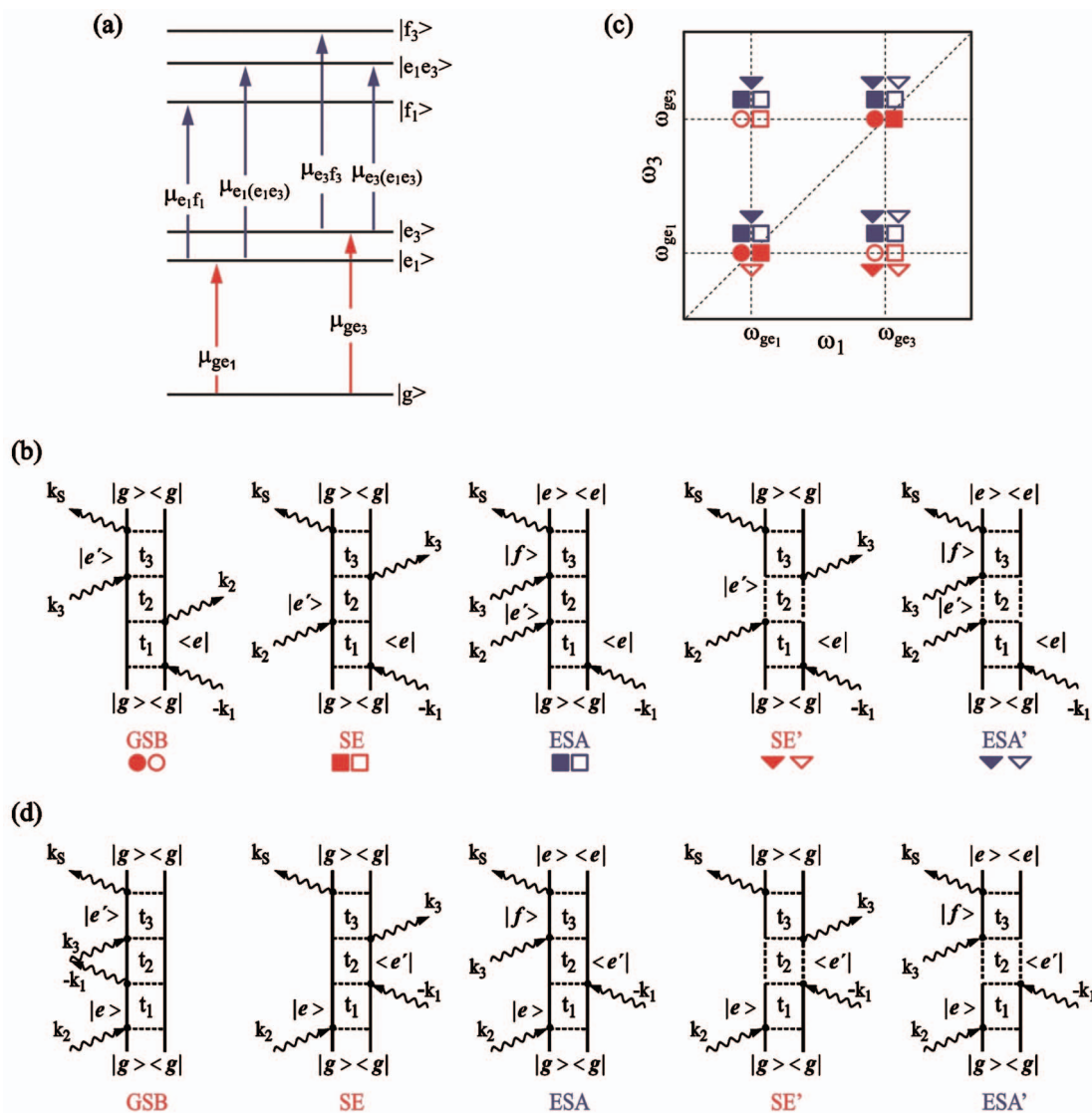
FIG. 4. (a) Five-level scheme consisting of two one-exciton states ($|e_1\rangle$, $|e_3\rangle$), two intraband two-exciton states ($|f_1\rangle$, $|f_3\rangle$), and one interband combination state ($|e_1e_3\rangle$) to schematically illustrate the level scheme used for numerical modeling of the data. For clarity only two coupled bands (I and III) are depicted. (b) Feynman diagrams illustrating Liouville space pathways for resonant three-pulse photon echoes in the RWA with (rephasing) wave-vector architecture $k_I = -k_1 + k_2 + k_3$. The graphs demonstrate four time-ordered pulse interactions (arrows) from bottom to top, while the two vertical lines show the density matrix state in each interval between the interactions with t_1, t_2, t_3 denoting the time delays between laser pulses. The first three diagrams describe processes in the absence of relaxation contributing to the PE signals. The labels on the diagrams represent the relevant manifolds of states: Ground state (g), single-exciton states (e, e'), and double-exciton manifold (f). Two additional diagrams including coherence and population relaxation during t_2 are depicted on the right (SE′, ESA′). (c) Schematic pattern of diagonal and off-diagonal peaks in 2D frequency-frequency space of a band-to-band interaction including the contributions of GSB (red circles), SE (red squares), and ESA (blue squares) and echo-intensities SE′ and ESA′ that result from coherence and population decay during t_2 (red and blue triangles). Full symbols refer to pathways where the system is in a population state during t_2, whereas open symbols indicate pathways including a coherence during t_2. (d) Nonrephasing Feynman diagrams in the RWA limit characterizing oFID-type signals (k_{II}).

tion with k_2, the system evolves either in the ground-state ρ_{gg} or in the one exciton manifold e either in population-space (ρ_{ee}) or in the coherent regime ($\rho_{ee'}$). Finally, the third interaction k_3 takes the system again into a one-exciton coherence (ρ_{eg}) or alternatively into a coherence between a one- and a two-exciton state (ρ_{ef}). The biexciton manifold essentially distinguishes the optical response of an excitonic aggregate from that of an electronic two-level system. Since the first two interactions can act on different one-exciton states, subsequent propagation of $\rho_{ee'}$ in the one-exciton manifold may involve electronic beating and quantum motion.[34,69] The diagrams cover three optical processes, thereby contributing to the overall signal via two initial interactions interrogated by

the k_3-pulse from left to right: Ground state bleaching (GSB), SE (both causing positive signals), and ESA, leading to negative signals. Diagrams SE′ and ESA′ with dashed pathways during time t_2 are extended graphs that account for exciton population relaxation and coherence decay. For combination transitions into the one-exciton interband states relaxation populates the low-energy band e and thus intensifies the low-energy cross-peak ($|\omega_1| > \omega_3$) and formation of its spectral streak. Figure 4(c) is a schematic sketch illustrating the intensities and details of absorptive 2D peaks in the rephasing photon-echo limit (k_I contributions). Diagonal and off-diagonal peaks stem from the coupled five-level system [Fig. 4(a)] and include the contributions of GSB (red circles),

SE (red squares), ESA (blue squares), SE′ (red triangles) and ESA′ (blue triangles). The correlation matrix contains the entirety of sequential transitions derivable exclusively from the rephasing Feynman graphs [Fig. 4(b)] with full (open) symbols denoting the density-matrix Liouville pathways for population (coherence) evolution during t_2, respectively. Note that the optimal diversification of optical pathways is expected in the $|\omega_1| > \omega_3$ domain of the low-energy cross signal. (Energy dispersive) exciton population relaxation into the low-energy band stimulates the SE′ and ESA′ processes from this level and thus causes the substantial intensity increase in the cross-peak signals and their spectral streaking below the main diagonal trace via combination transitions into both the one-exciton (positive absorption) and the two-exciton (negative absorption) bands, respectively. Aside from the k_I photon-echo spectrum, the full absorptive signal additionally contains contributions from nonrephasing k_{II} signal. Figure 4(d) illustrates the underlying Feynman graphs for nonrephasing k_{II} spectra.

In the absorptive correlation spectrum at $t_2=0$ fs [Fig. 5(a)] the various quantum pathways of sequential electronic transitions create positive peaks due to SE and GSB, and negative signals originating from ESA. The positive and negative contributions of bands I, II, and III are of equal strength, whereas band IV shows a weak positive absorption into the one-exciton state only. The positive signals dominate in the $|\omega_1| > \omega_3$ region (below the diagonal) with all four one-exciton bands being involved. The concomitant presence of strong ESA contributions of I, II, and III reflects strong transitions into two-exciton states, whereas band IV exhibits only very weak ESA processes. Since the ESA contributions of I, II, and III are blueshifted, interference of oppositely signed contributions gives rise to the observed asymmetry of the amplitude spectrum [Fig. 3], which can generally be taken as the fingerprint of coupled electronic oscillators. This effect is decisive for the initial skewness of the diagonal peaks in the amplitude spectra. So far, these features have been demonstrated in 2D studies only for the much simpler case of a single band J-aggregate.[70] In our multiband system all of the three main bands (I, II, and III) show this typical spectral signature of a molecular excitonic manifold of states with single- and double-exciton states.

In the off-diagonal regime of the spectrum the separated optical contours for positive (red) and negative (blue) absorption make disentangling of the various quantum processes less difficult than in amplitude spectra. We observe the predominant cross-peaks IV/II and III/I from strongly coupled bands IV and II and III and I, respectively. As outlined in the amplitude spectrum, both cross peaks originate from combination transitions, preferentially launched into the one-exciton interband states, with coordinates substantially located in the $|\omega_1| > \omega_3$ block and slightly stretched due to finite exciton population relaxation at $t_2=0$ fs. Note that early stretching can be readily mapped into a distribution of coupling strengths between band states and less collective tail-state absorbers from a disordered DOS that share common ground states. According to the sequential nature of biexciton preparation, two-exciton band-to-band couplings are tiny but not completely negligible at $t_2=0$ fs. Similar

arguments apply to the distorted line shape in the local vicinity of diagonal bands II and III, which is rotated from the diagonal and clearly reflects coupling of these states to band IV, with the cross-peak IV/II stemming from SE and GSB processes in the $|\omega_1| > \omega_3$ spectral region. Moreover, it is more than tempting to speculate that cross-peak III/II between closely located bands II and III spectrally overlaps the IV/II cross peak, which may explain the significant streaklike profile even at $t_2=0$ fs. Finally, ESA-peak I shows a small horizontal deformation at $t_2=0$ fs, thereby crossing the main diagonal and entering into the $|\omega_1| > \omega_3$ space. This is an indication of the beginnings of biexcitonic band-to-band coupling between bands I and III.

C. Dynamics of absorptive relaxation spectra ($t_2 > 0$ fs)

In Fig. 5(a) absorptive spectra recorded for $t_2=0$, 20, 50, 100, 200, and 500 fs demonstrate the quantum-kinetic road from initial quantum decoherence via ongoing exciton relaxation to increasing population transfer. The short coherence time of band IV (50 fs) sets a first boundary condition, which allows for an approximate factorization by dividing the relaxation into three dynamical regimes. Within the first 50 fs the onset of interband dephasing and exciton population relaxation leads to the disappearance of signal peak IV and this annihilation is paralleled by (i) a relative increase in the off-diagonal single exciton signal intensities (positive signals) among all bands in $|\omega_1| > \omega_3$ space and (ii) the appearance of biexciton couplings (negative off-diagonal signals), most significant bands III/I and IV/I. At t_2 times between 50 and 100 fs, ongoing population relaxation transforms the initial pattern of cross peaks into streaklike shapes. For $t_2 > 100$ fs, optical dynamics is mainly controlled by the irreversibility of relaxations from doorway states in the vicinity of bands II and III seeded by band IV via IV/III and IV/II off-diagonal traces, both from single-exciton (positive absorption) and biexciton (negative absorption) couplings. The peak intensities of the couplings steadily increase as a function of t_2 in the interval 100 fs $< t_2 <$ 200 fs and excitation transfer pathways begin to form, simply observable by following their spectral streakings and mapping out the most efficient relaxation channels. The cross-peak intensities converge because growing t_2 times of the analyzing third pulse (k_3) cause increasing interband dephasing. Thus, phase relaxation generates energy-distributed interband populations that increase cross-peak intensities and give rise to spectral streakings along coherence frequency ω_1. Vice versa, streaking off-diagonals witness uncorrelated single-exciton fluctuations as well as ongoing relaxations via intraband dephasing or interband mixing effects and are therefore a sensitive probe for tracing optical dynamics and the details of energy transfer. Extended Feynman diagrams in Figs. 4(b) and 4(d) (SE′ and ESA′) covering dephasing and population transfer between levels e and e' in the coupled scheme are quite useful. They allow to perceive off-diagonal streaking as a consequence of energy-dispersive interband exciton relaxation. The release of flowing populations promotes incoherent SE (SE′) and ESA (ESA′) as additional processes, which (particularly at
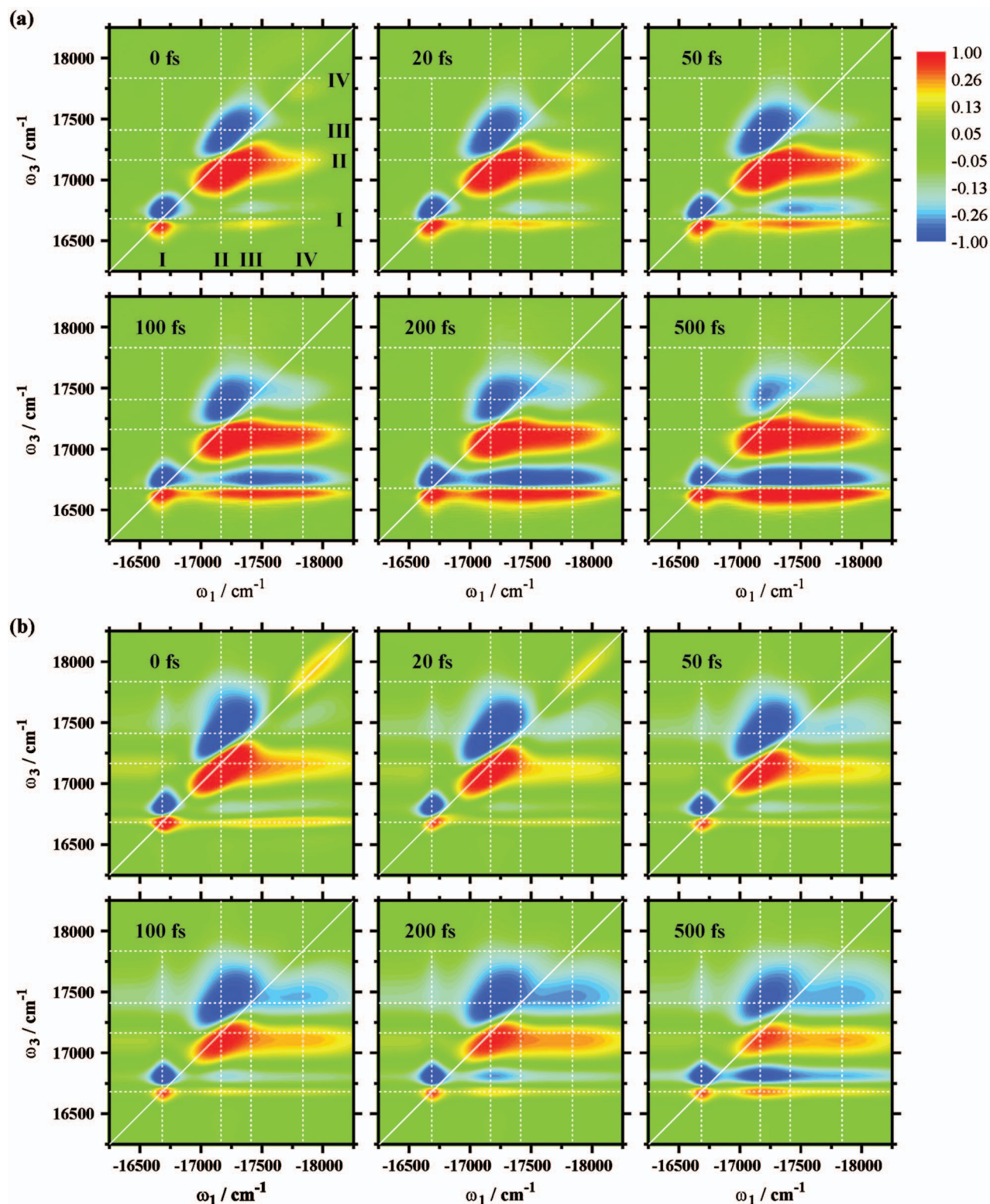
FIG. 5. (a) Experimental and (b) numerically calculated absorptive part spectra of C_8O_3 in water for t_2 times of 0, 20, 50, 100, 200, and 500 fs. All spectra are normalized to their respective maximum absolute value; color scale is based on a arcsinh-weighting function starting at $\sim \pm 5\%$ of signal intensity. Red peaks refer to positive absorption (SE, GSB) while blue colors indicate negative absorption (ESA).

room temperature) give rise to the systematic intensity increase in the low-energy cross-peak ($|\omega_1| > \omega_3$) and its spectral streaking. Note that also the diagonal peaks, due to their mutual couplings, leave the direction of the main diagonal trace and become parallel to the ω_1 axis. This is the second reason for the skewness of the diagonal peaks in the ampli-

tude spectra. Their pronounced elongation is quite natural, as the band transitions participating in the coupling process lose their identity due to the ongoing mutual erosion of their self-energies and the thermal release of populations into the $|\omega_1| > \omega_3$ space as a consequence of interband dephasing.

For $t_2 > 200$ fs, the 2D spectrum becomes mainly con-

trolled by relaxation of bands IV and III that start to transfer intensities into bands I and II. On this time scale, the off-diagonal intensities grow and tend to level off to the intensity of the diagonal signal amplitudes. On the 200–500 fs scale, the IV/II, IV/I, III/I, and II/I cross peaks reach intensities that match those of the diagonal signals. At these leveling-up points, the population gain in the band III manifold, due to coupling to IV, strengthens the quasicoalescence of coupling between III and II and triggers band II to band I transfer instantaneously seen by the occurrence of the off-diagonal II/I peak and its growth in intensity for $t_2 \gtrsim 200$ fs.

Overall, the basic steps of exciton interband pathways and tube-in-tube transfer are immediately comprehensible in 2D coherent electronic spectra without any preconceived bias. White arrows drawn in the amplitude spectra (Fig. 3) illustrate the predominant band-to-band couplings and population paths associated with the intercylinder transfer. One fast route to population gain in I stems from band III and IV via couplings III/I and IV/I in parallel single-step transfers. The second source term for the population of I proceeding from IV via couplings IV/III, III/II, and II/I is a migrational multistep process with the actual tube-to-tube spatial electronic transfer substantially delayed. Thus, phenomenologically, in both mechanisms the irreversibility of warm phonon exciton population relaxation is steering the energy flow to the inner tube 1 (band I) via directed funneling. More quantitatively, the relaxation physics describing the quantum dissipation of excitation energy transfer between the geometrical constraints of huge, mesoscopic excitonic tubes in close nanometric proximity is not trivial. A preliminary numerical approach to the problem that replaces the complex many-body of C$_8$O$_3$ through a multilevel system and includes both rephasing and nonrephasing terms in the reconstruction of the experimental data [Fig. 5(a)] is presented in Sec. VI.

V. REPHASING AND NONREPHASING CONTRIBUTIONS TO THE ABSORPTIVE SIGNAL

As already discussed in Sec. III, the time reversal in the scanning procedure of coherence time t_1, from negative to positive time delays, produces both $\boldsymbol{k}_I$ and $\boldsymbol{k}_{II}$ time-domain signals that contribute into the phase-matched direction to make up the total signal, i.e., a superposition of the photon-echo $\boldsymbol{k}_I$ and optical free induction decay (oFID) $\boldsymbol{k}_{II}$ profiles. In analogous frequency-frequency space, the absorptive 2D spectrum as (experimentally) obtained from (numerical and optical) double FT with respect to t_1 and t_3 evolutions of $\boldsymbol{k}_I$ and $\boldsymbol{k}_{II}$ data is the sum of the two signals according to Eq. (3). Based on the third order response function theory, each of them is given by the Fourier transformation of its corresponding response functions[30] (see also Sec. VI and Appendix),

$$E_{\boldsymbol{k}_j}^{(3)}(\omega_1, t_2, \omega_3) \propto i \int_0^\infty dt_1 \int_0^\infty dt_3 R_{\boldsymbol{k}_j}^{(3)}(t_1, t_2, t_3)$$

$$\times \exp(\pm i\omega_1 t_1 + i\omega_3 t_3); \quad j = \mathrm{I, II}. \quad (4)$$

Both $R_{\boldsymbol{k}_I}^{(3)}$ and $R_{\boldsymbol{k}_{II}}^{(3)}$ are causal and vanish for negative times t_1, t_2, t_3 and are built up by a different combination of optical

response pathways $R_1^{(3)}$, $R_2^{(3)}$, $R_3^{(3)}$, and $R_4^{(3)}$ in the conventional nomenclature[53]

$$R_{\boldsymbol{k}_I}^{(3)} = R_2^{(3)} + R_3^{(3)} - R_1^{(3)*},$$

$$R_{\boldsymbol{k}_{II}}^{(3)} = R_1^{(3)} + R_4^{(3)} - R_2^{(3)*}. \quad (5)$$

Note that according to the Feynman diagrams [cf. Figs 4(b) and 4(d)] the t_1 dependence of the $\boldsymbol{k}_I$ and $\boldsymbol{k}_{II}$ response functions has opposite sense of phase rotation and thus gives opposite ω_1 frequency sign after the Fourier transformations.

According to the above relationships, the rephasing ($\boldsymbol{k}_I$) and nonrephasing ($\boldsymbol{k}_{II}$) patterns have been experimentally obtained by reversing the order of arrival of pulses 1 and 2. Following a previous theoretical treatment,[60] one expects two limiting cases for the evolution of $\boldsymbol{k}_I$ and $\boldsymbol{k}_{II}$ data. For early t_2-times, shorter than the correlation time τ_c [in this limit the frequency correlation function $C(t)$ has not decayed much], the $\boldsymbol{k}_I$ echo signal is much more intense than the $\boldsymbol{k}_{II}$ one. For longer t_2-times, i.e., if there is no temporal overlap of pulse 3 with 1 or 2, the intensity of the $\boldsymbol{k}_{II}$ signal increases. For t_2-times larger than 100 fs the ratio of the rephasing/nonrephasing intensities is controlled by the loss of correlation memory of the echo signal, which is in accordance with numerical calculations.[71] Both $\boldsymbol{k}_I$ and $\boldsymbol{k}_{II}$ signals show their typical line shapes, while the former is elongated along the diagonal due to density matrix rephrasing; the latter is oriented into the direction of the antidiagonal.[58,59,72] Their sum is thus oriented horizontally for uncorrelated exciton states.

Figures 6(a) and 7(a) display the experimental 2D $\boldsymbol{k}_I$ and $\boldsymbol{k}_{II}$ line shapes for $t_2 = 0$, 20, 50, 100, 200, and 500 fs, respectively. The photon-echoes ($\boldsymbol{k}_I$) translate into diagonally elongated absorptive line shapes in 2D frequency domain [Fig. 6(a)], whereas the nonrephasing oFID terms ($\boldsymbol{k}_{II}$) become aligned along the antidiagonal axis in 2D-frequency space [Fig. 7(a)]. For waiting times up to 200 fs, the experimental $\boldsymbol{k}_I$ signal is much stronger than the nonrephasing one ($E_{\boldsymbol{k}_I}^{(3)} \times (\omega_1, t_2, \omega_3) / E_{\boldsymbol{k}_{II}}^{(3)}(\omega_1, t_2, \omega_3) \approx 3$). Conversely, for longer population times $t_2 > 200$ fs, the intensity of the $\boldsymbol{k}_{II}$ signal grows and both contributions nearly equalize in intensity in the asymptotic regime. Note, however, that the diagonal spectral line shapes of the rephasing echo data in Fig. 6(a) do not give symmetric line shapes, which is mainly due to the predominant interband exciton population dynamics in this system. Here, they become parallel to the ω_1 axis and streak for this reason, thereby featuring (in tandem with the cross peaks) electronic coupling, creation, and relaxation of interband excitons and tube-to-tube population transfer.

Finally, comparison of decomposed rephasing and nonrephasing 2D spectra reveals details of interband couplings and their different contributions to the overall ($\boldsymbol{k}_I + \boldsymbol{k}_{II}$) absorptive spectra [Fig. 5(a)]. Accordingly, one perceives that the early coupling between IV and II and its powerful streaking is mainly accessible to the rephasing wave-vector architecture and, to a major extent, is detected by the $\boldsymbol{k}_I$ photon-echo field. On the other hand, III/II coupling can be perceived better at longer t_2-times in both signals ($\boldsymbol{k}_I$ and $\boldsymbol{k}_{II}$), where the system has already lost much of its correlation. On the other hand, the effect of rephasing and nonrephasing
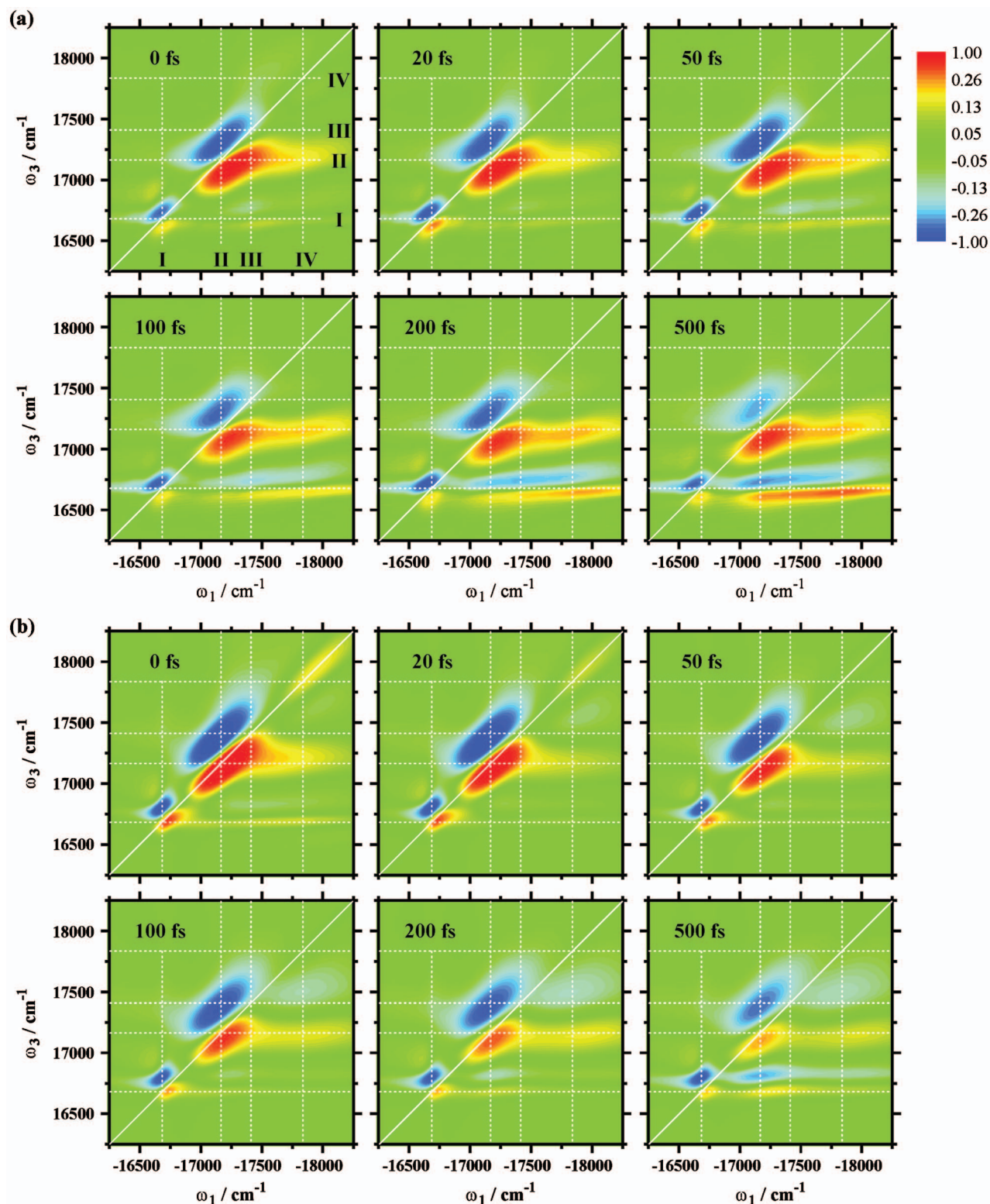
FIG. 6. Spectral decomposition of total 2D absorptive spectra (Fig. 5): Rephasing (k_I) 2D photon-echo spectra as function of waiting-time t_2. (a) Experiment and (b) simulation. See text for details.

pulse sequences is less pronounced for couplings IV/I and III/I. Simply, each of the IV/I and III/I cross-peak streakings from k_I and k_{II} data differs by tiny positive/negative slopes of equal size whose orientations (angle) relative to the ω_1 axis average out in the $k_I + k_{II}$ experimental spectra to yield the horizontal streak spectrum.

The phase-twisted line shapes may be used to disentangle the spectral convolution of band transitions II and III and thus to characterize, for the first time, the spectroscopic features of II, III and their role in wave-function mixing and electronic wave-packet motion due to band-to-band coherent coupling in the C_8O_3 architecture.[69] Since diagonal line-
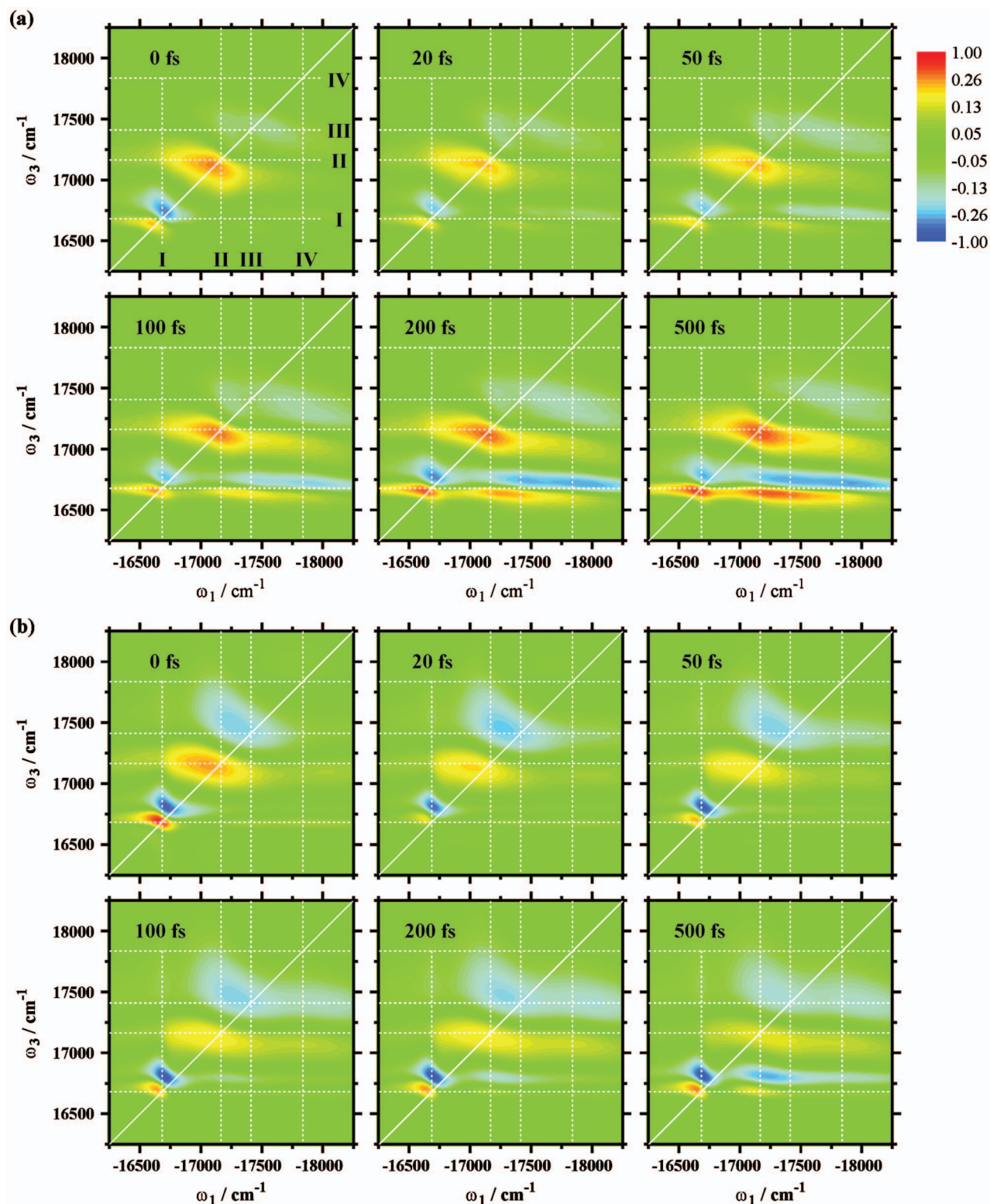
FIG. 7. Spectral decomposition of total 2D absorptive spectra (Fig. 5): Nonrephasing (k_{II}) 2D oFID-type spectra as function of waiting-time t_2. (a) Experiment and (b) simulation.

widths of individual transitions are narrower in the non-rephasing spectrum, they have the potential to spectrally resolve closely spaced diagonal and off-diagonal peaks usually concealed along the main diagonal trace of photon-echo data.[73] Quite obviously, the intense and inhomogeneously broadened peak II overlapping peak III in LA [Fig. 1(c)] becomes spectrally resolved in the k_{II} spectra. For t_2

≥ 50 fs a negative feature at the location of the cross-peak IV/III, indicative of coupling between IV and III, can be observed. Due to oppositely signed contributions (positive SE and GSB from IV/III and negative ESA from III/II) only the weak ESA contributions of IV/III coupling and the positive contributions of SE and GSB of III/II are visible. Generally, with the exception of this additional cross peaks and

the phase-twisted line shapes and their streaks, no distinct, additional peaks and streaks other than the ones observed in the experiments in Fig. 5(a) could be monitored in the k_{II}-regime. Note that the nodal line between positive and negative signals in the k_{II}-spectra is not perfectly perpendicular to the main diagonal but rotated off into the direction of the ω_1-axis due to the quasi-instantaneous fluctuations acting on the initial peak coherence.

VI. NUMERICAL SIMULATIONS

We have reconstructed the third order signal $E^{(3)}_{\text{abs}}$ $\times(t_1,t_2,t_3)$ and its double Fourier transform $E^{(3)}_{\text{abs}}(\omega_1,t_2,\omega_3)$ analog by theory and computational simulation.[30] The following procedures aimed to recover interband electronic couplings, exciton relaxation, and population transfer rely on the calculation of the third order optical response function.[53] The response function reflects all system properties relevant for the specific experiment through all possible system Liouville space pathways.

The 2D signal $E^{(3)}_{\text{abs}}(t_1,t_2,t_3)$ is proportional to the response function [Eqs. (4) and (5)]. A microscopic calculation of the response function $R^{(3)}(t_1,t_2,t_3)$ requires explicit information about the bottom-to-top architecture of C_8O_3 and the nature of its single- and double-excited eigenstates. The mesoscopic tubular aggregates dealt with in this contribution contain a huge number of molecules. A microscopic model that incorporates monomeric site disorder needs to contain at least roughly several thousands of coupled chromophores for a double-wall cylindrical structure with converged spectral properties (i.e., the spectra are independent of the length of the cylinder). For instance, for 1000 two-level molecules we obtain 1000 single-exciton states and $\approx 500\,000$ double-exciton states. The signal calculation would then have to involve threefold summation over these states. This rough estimate already precludes any atomistic-type approach for calculating nonlinear signals, thus being far beyond the currently available computational resources. However, the LA spectrum [Fig. 1(c)] suggests that only few optically active single-exciton bands are relevant. In order to represent the observed features and to quantify relaxation pathways and time scales, we therefore create an effective exciton model containing single- and double-excited states. These states represent the whole excitonic bands of the tubule, which show up in the absorption spectrum. The bands can be single or double excited, thus each band will be represented by an anharmonic oscillator. This will allow to implement an iterative fitting procedure of effective model parameters and will reveal the physical basis of the underlying processes. The system is represented by the Hamiltonian

$$\hat{H}_S = \hbar \sum_{e=1}^{4} \varepsilon_e \hat{B}_e^\dagger \hat{B}_e + \frac{1}{2}\hbar \sum_{e,e'=1}^{4} \Delta_{ee'} \hat{B}_e^\dagger \hat{B}_{e'}^\dagger \hat{B}_e \hat{B}_{e'}, \quad (6)$$

where $\hat{B}_e^\dagger$ is the Bosonic creation operator of the eth band exciton. The Hamiltonian parameters are the following: ε_e is the energy of the eth one-exciton band (determined from LA), $2\varepsilon_e + \Delta_{ee}$ is its biexciton energy, and $\varepsilon_e + \varepsilon_{e'} + \Delta_{ee'}$ is the energy of the state if the double exciton is distributed be-

tween the exciton bands e and e'. The quantity Δ gives the binding energies of different (or same) exciton bands and thus is the representation of exciton couplings: If all off-diagonal elements of the matrix $\Delta_{ee'}$ are zero, the Hamiltonian represents uncoupled oscillators and the 2D spectrum at zero delay time t_2 will have no interexciton cross peaks. Thus fitting of the 2D spectrum provides a handle to determine the matrix $\Delta_{ee'}$. This system is coupled to the laser field through the system-field interaction Hamiltonian

$$\hat{H}_{\text{SF}}(t) = -\sum_{e=1}^{4} \boldsymbol{\mu}_e \cdot \boldsymbol{E}_t(t)\hat{B}_e^\dagger + \frac{1}{\sqrt{2}}\boldsymbol{\mu}_e^{(2)} \cdot \boldsymbol{E}_t(t)\hat{B}_e^{\dagger 2}\hat{B}_e^\dagger + \text{H.c.},$$
$$(7)$$

where $\boldsymbol{\mu}_e$ is the transition dipole from the ground state to the single-exciton e and $\boldsymbol{\mu}_e^{(2)}$ is its correction for the transition from the single- to the double-exciton state. $\boldsymbol{E}_t(t)$ represents the total laser field. In the simulations we have assumed the same polarization for all pulses. The relaxation dynamics originates from the system-bath coupling represented by

$$\hat{H}_{\text{SB}} = \hbar \sum_{e=1}^{4} \sum_{\alpha} d_{e\alpha} \hat{B}_e^\dagger \hat{B}_e (\hat{a}_\alpha^\dagger + \hat{a}_\alpha), \quad (8)$$

where $\hat{a}_\alpha^\dagger$ and $\hat{a}_\alpha$ are the harmonic bath excitation creation and annihilation operators for the mode α and $d_{e\alpha}$ is the coupling strength between the mode α and exciton band e. For the infinite number of bath modes, we use the continuous bath spectral density reflecting uncorrelated fluctuations of transition energies

$$C_e''(\omega) = \pi \sum_{\alpha} d_{e\alpha}^2 [\delta(\omega - w_\alpha) - \delta(\omega + w_\alpha)], \quad (9)$$

where w_α is the characteristic frequency of αth harmonic bath mode. The specific choice of the spectral density reflecting the M-mode overdamped Brownian oscillator bath model uniquely defines the line shapes of both single- and double-exciton states. We then have

$$C_e''(\omega) \equiv \sum_{\alpha}^{M} 2\lambda_{e,\alpha} \frac{\omega \Lambda_\alpha}{\omega^2 + \Lambda_\alpha^2}. \quad (10)$$

Here the αth Brownian mode is characterized by the relaxation time scale of the bath correlations Λ_α^{-1} and the coupling strength between the eth oscillator and αth bath mode $\lambda_{e,\alpha}$. As a starting point, by examining the LA spectrum and identifying the four observed peaks I, II, III, and IV, we postulate four single-excited bands and represent them by four single-exciton states. Their transition energies and transition dipole moments (transition amplitudes) are deduced by using the decomposition of the experimental absorption spectrum into four Gaussian peaks by a least-squares fitting procedure, which provide a starting set of parameters. We note, however, that band I better corresponds to a Lorentzian line shape. To cover the spectral line shapes we couple each single-exciton state to two overdamped Brownian oscillator coordinates $(M=2)$.[74] The first (fast) will be responsible for the homogeneous linewidth (Lorentzian line shapes), while the second (static) will be responsible for the inhomogeneous linewidth (Gaussian line shape).

TABLE I. One-exciton state energies (ε_e), their transition dipoles [$\boldsymbol{\mu} = (x, y, z)$; $y = 0$ so we give just (x, z)], and system-bath coupling strengths (λ) for the two bath Brownian modes (the corresponding bath time scales $\Lambda_{fast}^{-1} = 50$ fs, $\Lambda_{slow}^{-1} = \infty$). Biexciton diagonal binding energies (Δ_{ee}), the biexciton state energies ($\varepsilon_f = 2\varepsilon_e + \Delta_{ee}$), and their transition dipoles (no combination states) are given as well. Note that here $\boldsymbol{\mu}_{ef} = \sqrt{2}\boldsymbol{\mu}_e + \boldsymbol{\mu}_e^{(2)}$.

Band	I	II	III	IV
ε_e/cm^{-1}	16 705	17 170	17 400	17 890
$\boldsymbol{\mu}_e$, (x, z)/a.u.	(0, 110)	(0, 136)	(66, 95)	(90, 148)
λ_{fast}/cm^{-1}	20	40	40	40
λ_{slow}/cm^{-1}	0	30	60	140
Δ_{ee}/cm^{-1}	150	250	50	0
ε_f/cm^{-1}	33 560	34 590	34 850	35 780
$\boldsymbol{\mu}_e^{(2)}$, (x, z)/a.u.	(0, 40)	(0, 20)	(0, 10)	(−9, −15)
$\boldsymbol{\mu}_{ef}$, (x, z)/a.u.	(0, 196)	(0, 212)	(93, 144)	(118, 194)

The LA spectrum is obtained by

$$\kappa_A(\omega) \propto \omega \, \text{Im} \int_0^\infty dt \, \exp(i\omega t) R^{(1)}(t), \tag{11}$$

where

$$R^{(1)}(t) = \frac{i}{3} \sum_e |\boldsymbol{\mu}_{eg}|^2 \exp(-i\varepsilon_e t - \gamma_{eg} t - g_{ee}(t)) \tag{12}$$

is the linear response function. $g(t)$ is the complex line-shape function originating from the system-bath interaction and is computed from the bath spectral densities as described in the Appendix. Note that system-bath couplings $\lambda_{e\alpha}$ induce the shifts in resonant absorption frequencies through $g(t)$. Additionally, we have tuned the transition dipole directions away from all-parallel alignment using linear dichroism data (not shown). This adjustment improves the fit of the 2D correlation signals described later. The adjusted parameters (transition energies, transition dipole amplitudes, and system-bath coupling constants) are listed in Table I, the resulting calculated LA being depicted in Fig. 1(c) gives a quite satisfactory fit to the experimental data.

Expressions of the $R_{k_I}^{(3)}$ and $R_{k_{II}}^{(3)}$ response functions can be written for an excitonic aggregate model with the ground state g, a single-exciton manifold e, and a double-exciton manifold f of the system eigenstates. We then have for the k_I response function[30]

$$R_{k_I, E}^{(3)}(t_1, t_2, t_3)$$

$$= \sum_{e_4 e_3 e_2 e_1} \langle (\boldsymbol{\mu}_{ge_4} \cdot \boldsymbol{E}_4(\bar{\omega}_4 + \omega_{ge_4})(\boldsymbol{\mu}_{e_3 g} \cdot \boldsymbol{E}_3(\bar{\omega}_3 - \omega_{e_3 g})$$

$$\times (\boldsymbol{\mu}_{e_2 g} \cdot \boldsymbol{E}_2(\bar{\omega}_2 - \omega_{e_2 g})(\boldsymbol{\mu}_{ge_1} \cdot \boldsymbol{E}_1(\bar{\omega}_1 + \omega_{ge_1})))) \rangle$$

$$\times \exp(-i\xi_{e_4 g} t_3 - i\xi_{ge_1} t_1 - \varphi_E^{(I)}(t_3, t_2, t_1)) \mathcal{G}_{e_4 e_3, e_2 e_1}(t_2), \tag{13}$$

$$R_{k_I, B}^{(3)}(t_1, t_2, t_3)$$

$$= \sum_{e_4, e_1} \langle (\boldsymbol{\mu}_{ge_4} \cdot \boldsymbol{E}_4(\bar{\omega}_4 + \omega_{ge_4})(\boldsymbol{\mu}_{e_4 g} \cdot \boldsymbol{E}_3(\bar{\omega}_3 - \omega_{e_4 g})$$

$$\times (\boldsymbol{\mu}_{e_1 g} \cdot \boldsymbol{E}_2(\bar{\omega}_2 - \omega_{e_1 g})(\boldsymbol{\mu}_{ge_1} \cdot \boldsymbol{E}_1(\bar{\omega}_1 + \omega_{ge_1}) \rangle$$

$$\times \exp(-i\xi_{e_4 g} t_3 - i\xi_{ge_1} t_1 - \varphi_B^{(I)}(t_3, t_2, t_1)), \tag{14}$$

$$R_{k_I, A}^{(3)}(t_1, t_2, t_3)$$

$$= - \sum_{f e_4 e_3 e_2 e_1} \langle (\boldsymbol{\mu}_{e_3 f} \cdot \boldsymbol{E}_4(\bar{\omega}_4 + \omega_{e_3 f})(\boldsymbol{\mu}_{f e_4} \cdot \boldsymbol{E}_3(\bar{\omega}_3 - \omega_{f e_4})$$

$$\times (\boldsymbol{\mu}_{e_2 g} \cdot \boldsymbol{E}_2(\bar{\omega}_2 - \omega_{e_2 g})(\boldsymbol{\mu}_{ge_1} \cdot \boldsymbol{E}_1(\bar{\omega}_1 + \omega_{ge_1}) \rangle$$

$$\times \exp(-i\xi_{fe_3} t_3 - i\xi_{ge_1} t_1 - \varphi_A^{(I)}(t_3, t_2, t_1)) \mathcal{G}_{e_4 e_3, e_2 e_1}(t_2), \tag{15}$$

where we have introduced the complex frequencies $\xi_{ab} \equiv \varepsilon_a - \varepsilon_b - i\gamma_{ab}$, (ab) density matrix coherence damping γ_{ab}, transition dipoles $\boldsymbol{\mu}_{ab}$ between exciton states a and b, zero-centered laser pulse spectral envelopes $\boldsymbol{E}_j(\omega)$ of pulses $j = 1, 2, 3, 4$, the pulse carrier frequencies $\bar{\omega}_j$, orientational averaging of scalar products $\langle \cdots \rangle$, time dependent correlation-damping phase functions φ, as well as single-exciton propagation Green's functions $\mathcal{G}$. These are described in the Appendix. "E" denotes SE, "B" as GSB, and "A" as ESA. Note that the response functions vanish for negative delay times. For the k_{II} response function we similarly get

$$R_{k_{II}, E}^{(3)}(t_1, t_2, t_3)$$

$$= \sum_{e_4 e_3 e_2 e_1} \langle (\boldsymbol{\mu}_{ge_4} \cdot \boldsymbol{E}_4(\bar{\omega}_4 + \omega_{ge_4})(\boldsymbol{\mu}_{e_3 g} \cdot \boldsymbol{E}_3(\bar{\omega}_3 - \omega_{e_3 g})$$

$$\times (\boldsymbol{\mu}_{ge_1} \cdot \boldsymbol{E}_2(\bar{\omega}_2 + \omega_{ge_1})(\boldsymbol{\mu}_{e_2 g} \cdot \boldsymbol{E}_1(\bar{\omega}_1 - \omega_{e_2 g}) \rangle$$

$$\times \exp(-i\xi_{e_4 g} t_3 - i\xi_{e_2 g} t_1 - \varphi_E^{(II)}(t_3, t_2, t_1)) \mathcal{G}_{e_4 e_3, e_2 e_1}(t_2), \tag{16}$$

$$R_{k_{II}, B}^{(3)}(t_1, t_2, t_3)$$

$$= \sum_{e_4 e_2} \langle (\boldsymbol{\mu}_{ge_4} \cdot \boldsymbol{E}_4(\bar{\omega}_4 + \omega_{ge_4})(\boldsymbol{\mu}_{e_4 g} \cdot \boldsymbol{E}_3(\bar{\omega}_3 - \omega_{e_4 g})$$

$$\times (\boldsymbol{\mu}_{ge_2} \cdot \boldsymbol{E}_2(\bar{\omega}_2 + \omega_{ge_2})(\boldsymbol{\mu}_{e_2 g} \cdot \boldsymbol{E}_1(\bar{\omega}_1 - \omega_{e_2 g}) \rangle$$

$$\times \exp(-i\xi_{e_4 g} t_3 - i\xi_{e_2 g} t_1 - \varphi_B^{(II)}(t_3, t_2, t_1)), \tag{17}$$

$$R_{k_{II}, A}^{(3)}(t_1, t_2, t_3)$$

$$= - \sum_{f e_4 e_3 e_2 e_1} \langle (\boldsymbol{\mu}_{e_3 f} \cdot \boldsymbol{E}_4(\bar{\omega}_4 + \omega_{e_3 f})(\boldsymbol{\mu}_{f e_4} \cdot \boldsymbol{E}_3(\bar{\omega}_3 - \omega_{f e_4})$$

$$\times (\boldsymbol{\mu}_{ge_1} \cdot \boldsymbol{E}_2(\bar{\omega}_2 + \omega_{ge_1})(\boldsymbol{\mu}_{e_2 g} \cdot \boldsymbol{E}_1(\bar{\omega}_1 - \omega_{e_2 g}) \rangle$$

$$\times \exp(-i\xi_{fe_3} t_3 - i\xi_{e_2 g} t_1 - \varphi_A^{(II)}(t_3, t_2, t_1)) \mathcal{G}_{e_4 e_3, e_2 e_1}(t_2). \tag{18}$$

A single-exciton propagation Green's function $\mathcal{G}$ describes the dynamics of the exciton density matrix in the single-exciton manifold. It is a solution of the generalized Pauli master equation which describes the decays of the density matrix coherences as a redistribution of populations. We used the secular form of the equation of motion as described in the Appendix. The Green's function is then given by
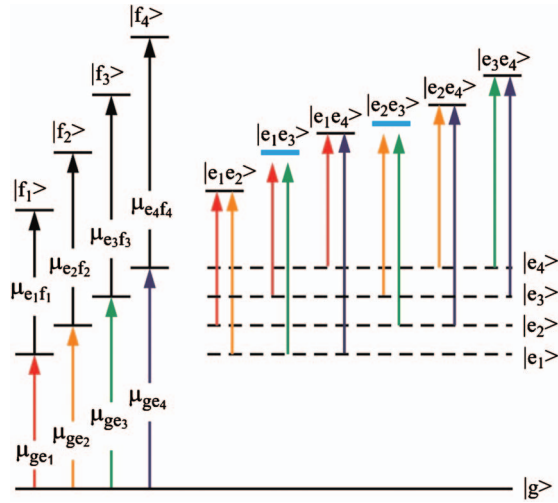
FIG. 8. Fourteen-level scheme consisting of four one-exciton states (e), four intraband two-exciton states (f), and six interband combination states (ee') to model the experimental data. Blue horizontal lines mark the combination transitions I–III and II–III at which an energy off-set needs to be introduced for satisfactorily recovering the experimentally observed coupling pattern.

$$
\begin{aligned}
\mathcal{G}_{e_4 e_3, e_2 e_1}(t) = {} & (1 - \delta_{e_4 e_3}) \delta_{e_4 e_2} \delta_{e_3 e_1} e^{-i\xi_{e_4 e_3} t} \\
& + \delta_{e_4 e_3} \delta_{e_2 e_1} [e^{-Kt}]_{e_4 e_2},
\end{aligned} \tag{19}
$$

where K is the population transport rate matrix: Its element $K_{e_4 e_2}$ denotes the exciton transfer rate from state e_2 to e_4, while the diagonal elements satisfy $K_{ee} = -\Sigma_{e'} K_{e'e}$. The population relaxation has been incorporated by specifying the transport rates between the single-excited states of the effective electronic oscillators, thus giving rise to lifetime broadening. The nonlinear signals are then calculated using Eqs. (13)–(18),[75] which allows to properly treat bath correlations and exciton transport, respectively. The fast mode of the Brownian oscillator is the main source of the exciton transport. The static mode induces spectral diffusion and is thus responsible for Gaussian spectral line shapes. The dephasing rates γ have been used to include only finite lifetime contributions to the dephasing. All other dephasing-correlation contributions enter through the line-shape functions φ and $g(t)$.

The calculation of the third order nonlinear response functions requires knowledge on biexciton states f and population transport rates. These are unavailable from the linear spectrum and there is no straightforward procedure to deduce biexciton states. However, the biexciton bands participate in shaping the 2D spectrum as their signals contribute as convolutions of single-exciton bands. Thus, we proceed with the model of coupled oscillators, which is equivalent to our primary estimate of four single-exciton states. Each oscillator is an exciton band, consequently has a corresponding biexciton band with the self-energy being close to twice the single-exciton energy. Thus, each exciton band is effectively a three-level anharmonic oscillator. The double excitations in the double-wall tubular system can be distributed among different exciton bands, thus the whole set of double excitons also includes interband excitations as the combination states. In Fig. 8 the complete 14-level scheme (four one-exciton levels of optically active excitonic bands, four biexciton lev-

TABLE II. Energies of combination bands ($\epsilon_{ee'}$) and their energetic off-sets ($\Delta_{ee'}$).

Combination band	I–II	I–III	I–IV	II–III	II–IV	III–IV
$\Delta_{ee'}/cm^{-1}$	0	50	0	250	0	0
$\epsilon_{ee'}/cm^{-1}$	33 875	34 155	34 595	34 820	35 060	35 290

els representing intraband double excitations, and six additional biexciton levels representing interband double excitations) which has been used to model the data is illustrated. This model is fully consistent with the Hamiltonian in Eq. (6). The fitting procedure of the biexciton manifold was performed using experimental 2D signals as follows. First, we consider $t_2 = 0$ delay so that exciton transport does not enter and keep all off-diagonal $\Delta_{ee'} = 0$ but vary only the diagonal elements Δ_{ee} to account for the intraband one- to two-band transitions associated with each of the bands I–IV. In this way the corresponding energetic positions and intensities are adjusted for best match of positive and negative contributions to the diagonal peaks in the 2D signal (cf. Table I). In a second step, to model the off-diagonal signal intensities induced by electronic interband couplings, we additionally tune the off-diagonal elements of $\Delta_{ee'}$ (Table II). This allows to uniquely determine the interband coupling strengths.

Iterative readjustment of population transfer rates among all of the bands I–IV involved in intertube transfer is taken into consideration for best numerical agreement with the experimental data at various delay times, i.e., optimum reconstruction of electronic couplings, relaxation rates, population streaking, and energy flow in terms of various Liouville space pathways of the density matrix trajectory and their corresponding optical response functions. Each of the data sets [Figs. 5(b), 6(b), and 7(b)] has been analyzed by the above simulation procedure to allow for comparison between experiment and theory. Note that in all calculations the theoretical response functions have been convoluted with the experimental Gaussian pulses to account for the finite width of the sub-20 fs pulse envelope taken from the experiment. Overall, the quality of the computational spectra compared to their experimental counterparts [Figs. 5(a), 6(a), and 7(a)] is good and comparable with the trends described in the literature.[58,59,72] The fit recovers the dynamical line shapes of diagonal and cross peaks quite adequately. The distinct line shapes of k_I, k_{II}, and absorptive $k_I + k_{II}$ signals have been reproduced as well.

A survival probability of an exciton state, given it is prepared in the initial state e, is given by $\mathcal{G}_{ee,ee}(t)$. Alternatively the survival time can be estimated using the population transport matrix. Its diagonal elements are the rates at which the exciton population is depleted from these states. Due to detailed balance the diagonal rate corresponding to state e is equal to the sum of all rates (along a column in Table. III) at which an exciton is transferred to all other states e'. For instance the rate $K_{IV,IV}$ of band IV covers a sum of exciton population loss times responsible for the population gain of bands III, II, and I. In Table. III we present inverse rates which correspond to the exciton survival times. We thus get τ_{IV} of 50 fs, τ_{III} of 174 fs, and τ_{II} of 403 fs. The 8.5 ps time

TABLE III. Interband exciton population transfer rates (in ps^{-1}) as derived from a four band model and an iterative fitting procedure of the experimental 2D spectra. To facilitate intuitive comparison, the arrangement of the relaxation rate matrix follows the frequency coordinates of the diagonal and off-diagonal peaks in the experimental spectra. An off-diagonal element of the shown matrix thus corresponds to the population transfer rate from a state indicated by the column into a state indicated by the row. According to the principle of detailed balance, the rates for uphill and downhill transfers (forward and backward rates) between two states are related by the Boltzmann condition (room temperature). Inverse lifetimes are given on the diagonal.

	I	II	III	IV
I	0.117	−1.20	0	0
II	−0.117	2.48	−4.03	0
III	0	−1.28	5.76	−20.0
IV	0	0	−1.73	20.0

scale of band I in our model is related to the thermally activated uphill energy transfer. This is because we do not include exciton relaxation to the ground state. The calculated rates presented in Table. III demonstrate the downward energy transport IV→III, III→II, and II→I. The fastest pathway with a rate of 50 fs is associated with IV→III, where energy transfers from the peripheral excitons to the excitonic band of the tube core. This equilibrates in ∼200 fs through the III→II pathway. The final relaxation into band I (≈400 fs) is the slowest step. For this reason it is legitimate to state that the balance between bands III and II remains intact even with the II→I transfer process.

VII. DISCUSSION

In this work, 2D coherent electronic spectroscopy has been applied to the tube-to-tube excitonic energy transfer in the double-wall cylinder aggregate C_8O_3. Correlation measurements of exciton absorption (ω_1) and emission (ω_3) frequencies have experienced a new dimension in the perception of the underpinnings that cause exciton scattering and population transfer. Cross-peak signals reflecting double-quantum combination transitions of spatially close transition dipoles and predominantly emerging in the low-energy off-diagonals ($|\omega_1| > \omega_3$) of the (asymmetric) correlation matrix provide a direct image of electronic coupling and early quantum dissipation, model-free, and without any preconceived bias. The cross signals for snapshots at waiting-times $t_2 = 0$, 20, and 50 fs [cf. Fig. 5(a)] illustrate the first steps of interband exciton dynamics smoothed by finite-pulse spectral convolution and very early electron-phonon dephasing. The initial electronic interband coherence is subjected quasi-instantaneously to dissipative terms of pure and lifetime dephasing which rigorously damp out oscillatory amplitudes on time scales of $t_2 > 20$ fs. With increasing waiting-time $t_2 > 50$ fs and ongoing population relaxation, the off-diagonal peaks (read out by pulse k_3) translate into characteristic streaking patterns, which become oriented parallel to the ω_1-coordinate and are moderately broadened along the ω_3-axis. The formation of these stretched contours, which are especially significant in large excitonic molecular many-body systems, can be understood through increasing inter-

band relaxation that populates exciton band I as t_2 elapses. Therefore, population flow gives rise to additional SE′ and ESA′ contributions which cause the cross-peak intensity of the echo signal to increase and to streak.

Moreover, due to admixtures of static site disorder, the oscillator strengths in the C_8O_3 aggregate partly fluctuate and lead to a dispersion of less collective, weakly absorbing tail states (with a common ground state). While t_2 evolves, the DOS tail-state excitations undergo energy-dispersive transfer. This type of spectral diffusion changes the first (central mean) and the second moment (width) of their frequency fluctuation and, as a consequence, causes the tail states to energetically spread along the main diagonal $|\omega_1| = \omega_3$. They couple to excitonic band dipoles via correlated combination transitions and are read out by the third interaction k_3 to yield cross-peak intensities proportional to the product of the squared transition dipoles ($|\mu_i|^2 |\mu_j|^2$) from both the (distributed) local tail states ($|\mu_i|^2$) and the respective excitonic band states ($|\mu_j|^2$, e.g., the J-band I). Since the population tail states evolve in frequency as a function of the waiting time, this explains spectral streaking and the pronounced increase in cross-peak intensity with ongoing relaxation as long as one of the states is a strong absorber (in our case band I), even if the transition moment of the corresponding diagonal signal (tail states of band IV) is weak (intensity stealing).[76] Streaked cross signals in 2D experimental excitonic data and their intensity growth are therefore a sensitive probe to trace relaxation processes and explicate electronic coupling, quantum dissipation, and transfer simply by looking into the typical dynamic motifs of off-diagonal streaking as a function of the waiting-time t_2. In Fig. 5(a) the absorptive spectra and their streaked coupling patterns image these processes. They provide a pictorial description of molecular interband excitonics that follows distinct quantum-dissipative Liouville pathways [cf. Figs 4(b) and 4(d)].[30,53]

A. Electronic coupling patterns and pathways of excitonic energy transfer

The 2D experiments shown in Figs. 3 and 5 demonstrate that the exciton tube-to-tube transfer across the space-energy landscape of band dipoles I–IV is a network of delicately balanced intraband mixing, single-step energy transfer, and migrational band-to-band processes that overall determine the distinct quantum-dissipative signature of excitation energy flow in C_8O_3. In Fig. 3 white arrows in the amplitude spectra sketch the roads of energy-space excitonic interband signatures driven by the interplay of interband couplings and interband population relaxation for distinct waiting-times t_2. Recall that even at $t_2 = 0$ fs cross peaks between bands IV/II and III/I are observed. For t_2 delays of 50 and 100 fs additional transfer from IV and II to I leads to the pronounced streaklike profile of the cross peaks associated with I. Finally, for $t_2 = 200$ and 500 fs, the tube-to-tube transfer from II to I completes the cascade of downhill energy transfer. Thus it is striking that population of I via the II/I coupling pathway between outer and inner cylinder coordinates is strongly delayed compared to the cross-peak gain of I via direct III/I coupling. Quite obviously, the initial (delocalized) macroco-

herence tries to find the optimum coordinates for the outer (2) to inner tube (1) population transfer, and this reorganization of excitations must proceed via the migrational, multi-step mechanism which costs time.

2D spectroscopy thus reveals that the dynamics of the downhill energy flow in C_8O_3 is no trivial irreversible funneling process, but quite obviously complicated by single-step source terms that make the kinetics more complex. More strictly, it is the spatioelectronic architecture of inter-cylinder excitations and their combination states that predetermines the nature of couplings. Particularly in the proximity of bands II and III, spatioenergetic factors, phenomenologically similar to those in the FMO complex,[32] seem to create a kinetic bottleneck with a significant increase in the exciton dwell time and population density numbers in II/III bands prior to the final event of II→I outer- to inner-tube transfer. This becomes evident by inspection of the absorptive spectra in Fig. 5(a). For $t_2 > 200$ fs, the population gain in the band III manifold due to relaxation from IV strengthens the quasicoalescence of coupling between bands III and II, and finally opens the gate to tube-to-tube transfer on the 200–500 fs time scale, paralleled by the appearance of the II/I low-energy off-diagonal peak. On this time scale, one looks into the avenue of incoherent excitation transfer and sees its quantum-dissipative past simply by qualitative inspection of the streaking off-diagonals and the temporal change in their varying streak lengths. These particulars and details impressively illustrate why 2D-ES is superior to other third order techniques. Energy-selective excitation in PP experiments[40] bears a tradeoff in time resolution, whereas the 2D-ES technique allows to exploit broad spectral bandwidths and short temporal widths of ultrafast excitation pulses in one and the same experiment.

Moreover, additional insights into the nature of the high-energy, diagonal absorber IV and its unique role as a powerful mediator of optical funneling have been gained in this 2D-ES study. Quite obviously, its ultrafast deactivation has decisive impact on the early relaxation regime ($t_2 < 50$ fs) which dramatically affects the patterns of initial cross peaks in the subsequent optical dynamics. Despite its short-lived (50 fs) correlation lifetime, the electronic communication of band IV (assigned to an intertube ensemble accounting for the suprastructure) is far reaching and persistent, and its huge coupling efficiency creates a network of exciton source terms in the forefront of band II to band I transfer as discussed above. 2D spectra are sensitive to nonlinear fluctuations, so they show that the molecular organization of transition IV must differ from those in I, II, and III, i.e., band IV is less compact and more exposed to environmental bath dynamics which may explain its short correlation survival time. It is therefore tempting to assume that band IV is at least a partially symmetry-broken ensemble expressed by a typical DOS of distributed (localized) levels and transitions that are no longer collective but correspond to individual molecular dipoles with the usual oscillator strengths. For this reason, in particular the very early streaks of off-diagonals IV/I and IV/II along the ω_1-axis, basically controlled by dominating GSB/SE optical transitions at $t_2 < 50$ fs, are striking examples of DOS-induced relaxation as a consequence of band IV symmetry breaking and exciton-phonon coupling.

On the 200 fs time scale, the interband relaxation transfers populations into the electronic arrival states, both from linear and nonlinear dipole transitions and correlated combination transitions from a common ground state. Note that the presence of both positive and negative contributions to the cross peak provides strong evidence that one and the same two-exciton state can be reached from different one-exciton manifolds. For example, it becomes evident from the absorptive k_{II} spectrum at $t_2 = 200$ fs that bands III and II are coupled to each other (concealed cross-peak III/II) and each of them to band IV (IV/III, IV/II). In particular, IV/II demonstrates substantial streakings via GSB/SE single-exciton and ESA biexciton band-to-band relaxation. Consequently, the latter gain terms increase the SE/GSB and the ESA-photon-echo intensities as relaxation evolves. Population flow into III thus causes the intensity growth of the off-diagonal streaking of III/I and IV/III for both single- and biexcitonic transitions.

B. Numerical computation revisited

Evaluation of relaxation controlling the quantum kinetics of excitation energy flow to the inner tube 1 (band I) is not a trivial task, and only a preliminary solution to the problem was given in Sec. VI. Perturbational, semiclassical solutions to the 2D FWM nonlinear response theory[53,74,77] by numerical computation in iterative fit and compare cycles in conjunction with an effective 14 level scheme (Fig. 8) have been used to reconstruct experimental 2D spectra. Bath-induced fluctuations of energy levels determine the linear line shapes, whereas 2D spectra are furthermore sensitive to correlations between various level fluctuations (cf. Appendix). In the present model, we have assumed that the bath-induced fluctuations of the single- and double-excited states of each effective oscillator are fully correlated, whereas for different oscillators the fluctuations of levels are uncorrelated. Within these assumptions, the line-shape functions for the double-excited states can be uniquely deduced from the line-shape functions of the single-excited states. The model parameters are listed in Tables I–III.

Contrary to a preliminary evaluation,[78] analysis of the experimental 2D spectra has been performed here using experimental Gaussian pulse envelopes in the calculation of the optical response and taking into account both rephasing photon-echo (k_I) and nonrephasing (k_{II}) data. Figures 6 and 7 show the rephasing and nonrephasing signals in comparison with theory and experiment, while Fig. 5 displays their summation. The k_I and k_{II} signals show their unique line shapes: The k_I line shapes are elongated along the diagonal due to density matrix rephasing, whereas the k_{II} patterns show antidiagonal orientation, both resulting in relatively horizontal elongation in the line shapes of the sum. Both field sequences are sensitive to combination transitions and coupling with cross peaks parallel (k_I) or perpendicular (k_{II}) to the main diagonal trace and quasihorizontal in the sum ($k_I + k_{II}$).

The simulation of the relaxation spectra recovers the off-

diagonals and their streaking features quite satisfactorily. Moreover, the decay of diagonal intensities is adequately reconstructed for longer times t_2. Aside from sorting into different pathways in different wave-vector combinations, this results from a reevaluation of the density of exciton states in C_8O_3. In Ref. 78 we have used a single fast overdamped Brownian oscillator with $t=50$ fs relaxation time scale to account for spectral line shapes. This assumption was based on the observation that the first exciton band is Lorentzian, in very good agreement with a reasonable system-bath coupling (20 cm^{-1}). However, for the broader high-energy bands this fixation yielded very broad, relatively circular, and thus low-intense peaks at large t_2 delay times. By contrast, the experiments show that the high-energy peaks remain elliptical and quite strong at all delay times. Therefore, we have attributed the high-energy exciton bands (III and IV) to correspond to the high density of exciton states, which are highly inhomogeneous (as a consequence of additional structural and energetic disorder in the aggregate). To capture this we have modified our bath model to include both fast (50 fs) and slow (static) Brownian oscillators. To accommodate new reorganization energies we have adjusted the single state energies and their transition dipoles to fit the absorption and double-exciton binding energies to fit the 2D spectrum. The 2D calculations in Fig. 5(b) now yield narrower exciton bands across the main diagonal of high-energy exciton bands (II–IV). The population transport rates are such that population from band IV goes to III and then to II, where it stays for up to 500 fs. In the spectrum this is observed through fast decay of bands IV and III and slow decay of band II, which is in accordance with the experiment (cf. Sec. IV). The spectral line shapes in I and II remain elliptical, i.e., the 2D spectra now show more distinct diagonal elongation of peaks, representing inhomogeneously broadened exciton resonances.

The simulation method outlined in this work enables to quantify the coupling and relaxation pattern of the system and thus to find a useful, first approximation to the problem of coupled high-dimensional excitonic tubes, basically untractable in an *ab initio* atomistic treatment. To close, note that the effective level scheme (Fig. 8) immediately explains band-to-band coupling and its origin due to double-quantum combination transitions. From this point of view, fields can act on two different single-excited states (say $|e_1\rangle$ and $|e_2\rangle$), which can be seen as a double-excited combination transition $|e_1e_2\rangle$. The contributions of these combination transitions exactly cancel in the case of noninteracting single-excited states, i.e., when (i) the transition moments are kept (i.e., μ_{ge_1} connects $|e_1\rangle \rightarrow |e_1e_2\rangle$ and μ_{ge_2} connects $|e_2\rangle \rightarrow |e_1e_2\rangle$) and (ii) the energy of the double-excited (combination) state matches the sum of the two states involved. By shifting the combination transition energy, one can eliminate this cancellation and induce a cross peak. This corresponds to "exciton-repelling/attracting" interactions.[79] Note that the 2D spectra calculated this way are very sensitive to the shift and thus provide a good test for the coupling pattern between the aggregate bands. It is remarkable that the experimental peak pattern is reconstructed if band IV has zero coupling with other bands; the weak shoulder at IV/II crossing at short delay times may be attributed to a continuation of a strong

inhomogeneously broadened III/II cross peak. While the diagonal value of Δ of IV band is 0 as well, the diagonal peaks survive due to asymmetry of their transition dipoles, which indicate that band IV has properties of a two-level electronic oscillator with weak signatures of excitonic interactions. The III–IV and I–IV cross peaks emerging at later delay times are mostly related to population flow in the aggregate.

VIII. CONCLUSIONS AND OUTLOOK

Our measurements have shown that coherent 2D electronic spectroscopy in absorption/emission (ω_1, ω_3) frequency correlation maps produces a novel quality of molecular interband spectroscopy in the visible optical transition regime. We have demonstrated how 2D-ES can be used to trace electronic coupling, single-step, and sequential band-to-band energy transfer and, combined with model simulations, reveal transfer rates for the energy-space excitation flow in a multiband aggregate. This paper is the first rigorous, experimental/theoretical work applied to the puzzle of ultrafast correlations in the tubular aggregate C_8O_3, in aqueous solution and at room temperature, for cross signals measured at the shortest wavelength reported so far. Only a few 2D studies on molecular systems in the visible spectral range exist so far,[29,32–34,45,69,70,78,80] since 2D electronic transitions in the high-frequency optical cycle regime are more difficult to manipulate compared to their vibrational (IR) counterparts.[81]

In our experiments, low-energy cross peaks in the correlation maps (triangle below the main diagonal) highlight weakly relaxing, electronic interband coherence for early waiting times $(t_2 < 20$ fs$)$. The existence of these off-diagonal signals at room temperature is surprising and may be attributed from a molecular/stereochemical point of view to the reduced fluctuations in the hydrophobic interface between the two cylinders which lengthens the survival time of the coherent memory in the intertube, energy-transfer regime. The oscillatory amplitudes of the coherent kernel, however, have not been observed in comparison with the long-lasting coherent quantum motion in the biological FMO complex at low-phonon temperature.[34] Rather, the ongoing streaking of the cross peaks in conjunction with the continuous growth of their signal intensity is the striking observable that is dominating our experiments for waiting-times $t_2 > 50$ fs. Spectral streaking of 2D absorptive spectra in C_8O_3 is the typical dissipative signature of electronic coherence loss due to energy-dispersive exciton population triggered by uncorrelated fluctuations of exciton bands. Off-diagonal interband phase relaxation generates continuously increasing intercylinder populations for lack of depopulation channels (fluorescence) on this ultrafast time scale (and in the absence of exciton annihilation). When read out by pulse k_3, they are launched into both coherent and incoherent doorway states whose super-radiant transitions give rise to growing signal intensities and spectral streaking.

Vice versa, cross peaks and their early streak formation have ground-breaking diagnostic impact on the visualization of the various stages of interband coherence loss and quantum dissipation. Both amplitude (Fig. 3) and absorptive part

spectra (Fig. 5) provide a direct and complementary time-resolved view on the entirety of the typical dynamic motifs describing the overall quantum-kinetic (non-Förster-type) energy-space transfer in this aggregate system, i.e., initial band-to-band delocalization, interband dephasing, coupling, and on longer time-scale ($t_2 > 200$ fs) energy transfer in population space between the inner and outer wall tubules, quasimodel-free, and without preconceived bias. These experiments are therefore superior to spectrally resolved PP spectroscopy. One advantage is that 2D-ES as a phase-locked and time-resolved heterodyne FWM technique uses three excitation pulses, so that a clear timing axis for coherence time t_1 exists along which the time ordering of the first two pulses can be interchanged. This leads to rephasing photon-echo spectra $E_{k_I}^{(3)}(\omega_1, t_2, \omega_3)$ and nonrephasing spectra $E_{k_{II}}^{(3)} \times (\omega_1, t_2, \omega_3)$ derived from the oFID $E^{(3)}(t_1, t_2, t_3)$. Both spectra give the couplings, but the time-ordered k_I photon echo spectra eliminate inhomogeneous broadening (IHB) and factorize both types of dephasing HB and IHB in one and the same experiment. On the other hand, the antidiagonal k_{II} data with phase-twisted line shapes have narrower diagonal linewidth which helped to identify, for the first time, the orthogonal band III (congested in the k_I data) as a (low-intense) disentangled absorber on the main diagonal. Another advantage over 2D PP is close at hand. Since the complex 2D correlation spectra $E_C^{(3)} = E_{abs}^{(3)} + i E_{dis}^{(3)}$ are obtained from a sum of k_I and k_{II} data $E_C^{(3)} = E_{k_I}^{(3)}(\omega_1, t_2, \omega_3) + E_{k_{II}}^{(3)}(\omega_1, t_2, \omega_3)$, the two types of signals serve to eliminate the dispersive part in favor of the pure absorptive part. Finally, spectrally resolved PP spectroscopy interrogates the intensity dynamics of excited bands I, II, III, and IV and measures the tube-to-tube transfer via population transfer.[42] Thus the technique reflects the incoherent, downhill population flow from IV to I along the main diagonal trace, as it was shown by PP simulations for directed energy transfer in a two-exciton manifold.[82] 2D-ES, however, spans up the entirety of diagonal and off-diagonal signals along the rectangular triangles in ($|\omega_1| < \omega_3$) space of the correlation matrix below the main diagonal trace and thus measures time-dependent ω_3-ω_1 correlations not only along the hypotenuse (diagonal peaks) but also the cross peaks along the horizontal and vertical cathete (off-diagonal peaks and streaks). 2D-ES thus reveals the real underpinnings of population transfer in C_8O_3, i.e., electronic coupling/wave-packet motion[34,69] and early electron-phonon/exciton-population scatter. A similar quality with comparable information content may emerge by the very recent and elegant 2D-PP advancement in Zanni and co-worker.[83] In this configuration the pump is a double pulse which—phase locked and time delayed in a pulse shaper—opens variable timing between pulse replicas 1 and 2 along t_1 coherence time. Interrogation via the probe pulse yields the measuring signal as a convolution of the double-pulse coherence and the probing field in frequency-frequency space without using an additional LO and the phasing procedure.

In closing, our 2D-ES studies have shown that the organic bitubular C_8O_3 aggregate with nanoscopic interwall dimensions and several hundreds micron cylinder length behaves as a short-lived mesoscopic quantum system with sig-nificant interband energy transfer pathways making this self-assembled system a promising candidate for an artificial light-harvesting device at room temperature. C_8O_3 has beautiful symmetries and is an ideal model system for studies on chirality related interband excitonic phenomena by using multidimensional spectroscopy. In general, shaped pulses generate different polarization target areas, while polarized pulses with variable vertical and horizontal planes in 2D experiments[33,84] imprint variations in the diagonal and off-diagonal traces of the correlation spectrum. In any case, they are modifying the quantum memory kernels of interband couplings[85] which may affect the details of energy-space-time pathways of interband excitons. Such cross-peak specific 2D-ES experiments on bitubular C_8O_3 and derivatives in combination with atomistic computations based on a chiral Hamiltonian are on the way.

APPENDIX: CORRELATED PROPERTIES OF A NONLINEAR MULTIBAND SYSTEM

1. Obtaining model parameters from the linear and 2D spectra

The linear optical properties of the model are given by the transition energies of each oscillator ε_e and the corresponding transition dipoles $\boldsymbol{\mu}_e$ which constitute the single-exciton manifold e. The 2D spectrum is a fingerprint of *nonlinear* properties of the whole system described by Eqs. (6)–(10).[30] The model has been adapted for the tubular aggregate in Sec. VI. The nonlinearity of the model is imprinted in the properties of the double-exciton states. The doubly excited states can be separated into two groups. (i) The double excitations of the eth oscillator, $f \equiv (ee)$. They have energy $2\varepsilon_e + \Delta_{ee}$. (ii) The doubly excited intermode state of the whole system when two oscillators e and e' are single excited (so-called combination state), $f = (ee')$, $e \neq e'$. Such states have energy $\varepsilon_e + \varepsilon_{e'} + \Delta_{ee'}$. Each oscillator can be excited to its own doubly excited state $f = (ee)$ only from its single-excited state e with the amplitude of this transition being the dipole $\boldsymbol{\mu}_{e,(ee)} = \sqrt{2}\boldsymbol{\mu}_e + \boldsymbol{\mu}_e^{(2)}$. The transition dipole from the single excited state of the oscillator e into the combination state $f = (e'e'')$ $e' \neq e''$ is given by $\boldsymbol{\mu}_{e,(e'e'')} = \delta_{ee'}\boldsymbol{\mu}_{e''} + \delta_{ee''}\boldsymbol{\mu}_{e'}$. These spectroscopic parameters are sufficient for the characterization of nonlinear properties of the coupled oscillator model. The spectral peak positions and amplitudes are now determined by ε, $\boldsymbol{\mu}$ (these affect the LA and the 2D spectra) and Δ, $\boldsymbol{\mu}^{(2)}$ (which affect only 2D spectra). To account for correlated spectral line broadening, each effective oscillator is coupled to an overdamped Brownian oscillator given by Eq. (8). This results in fluctuations of system Hamiltonian parameters. Fluctuations of eigenstate energies

induce spectral broadenings. For the whole system this results in the matrix of the line-shape functions g_{ab}, which characterize correlated fluctuation of transition energies of a and b global states. The line-shape function is related to the fluctuation correlation function as described in Ref 53. For our model of a set of Brownian coordinates [see Eq. (10)] the line-shape function is given by

$$g_{ab}(t) = \sum_{\alpha}^{M} \frac{\lambda_{ab,\alpha}}{\Lambda_\alpha}\left(\frac{2k_BT}{\hbar\Lambda_\alpha} - i\right)(\exp[-\Lambda_\alpha t] + \Lambda_\alpha t - 1). \tag{A1}$$

We assume that the bath induces uncorrelated fluctuations of transition energies of the oscillators. In this case for our model described by Eqs. (6)–(10) the $\lambda_{ab,\alpha}$ parameters can be easily expressed using the oscillator fluctuation parameters $\lambda_{e,\alpha}$ in Eq. (10). We then get the global eigenstates as follows: $\lambda_{ab,\alpha}=0$, if one a or b is the ground state g. Within the single-exciton manifold only

$$\lambda_{ee,\alpha} = \lambda_{e,\alpha} \tag{A2}$$

are not zero.

For the off-diagonal part if a is within e (single-exciton) manifold and b is within f (double-exciton) manifold we have

$$\lambda_{e(e'e''),\alpha} = (\delta_{ee'} + \delta_{ee''})\lambda_{e,\alpha}. \tag{A3}$$

Here the e state corresponds to the single excitation of the eth oscillator, the f state is either the combination state $e' \neq e''$ or the overtone state $e'=e''$. Finally, for the line-shape functions in the double-exciton manifold we have

$$\lambda_{(e_1e_2)(e'e''),\alpha} = (\delta_{e_1e'} + \delta_{e_1e''})\lambda_{e_1,\alpha} + (\delta_{e_2e'} + \delta_{e_2e''})\lambda_{e_2,\alpha}. \tag{A4}$$

The fluctuation-induced line-shape functions φ for each pathway in Eqs. (13)–(18) account for their correlated dephasing and relaxation. Based on the results of previous work[30,75] we use cumulant expansion techniques, where we properly account for coherent and population dynamics and take care of correlated bath fluctuations between various time intervals. Thus we obtain the respective fluctuation induced line shapes. The spectral broadening correlation functions for the third order response in Eqs. (13)–(18) are given in terms of the line broadening functions $g(t)$,

$$\varphi_E^{(\mathrm{I})}(t_1,t_2,t_3) = \delta_{e_2e_4}\phi_{e_4ge_1}^*(t_1,t_1+t_2+t_3,t_1+t_2,0)$$

$$+ (1-\delta_{e_2e_4})\bar\phi_{e_4ge_4e_1}^*(t_3,t_2,t_1), \tag{A5}$$

$$\varphi_B^{(\mathrm{I})}(t_1,t_2,t_3) = \phi_{e_3ge_1}^*(t_1+t_2,t_1+t_2+t_3,t_1,0), \tag{A6}$$

$$\varphi_A^{(\mathrm{I})}(t_1,t_2,t_3) = \delta_{e_2e_4}\phi_{e_4fe_1}^*(t_1,t_1+t_2,t_1+t_2+t_3,0)$$

$$+ (1-\delta_{e_2e_4})\bar\phi_{fe_4e_4e_1}^*(t_3,t_2,t_1), \tag{A7}$$

$$\varphi_E^{(\mathrm{II})}(t_1,t_2,t_3) = \delta_{e_2e_4}\phi_{e_4ge_1}(t_1,t_1+t_2,t_1+t_2+t_3,0)$$

$$+ (1-\delta_{e_2e_4})\bar\phi_{e_4ge_4e_1}(t_3,t_2,t_1), \tag{A8}$$

$$\varphi_B^{(\mathrm{II})}(t_1,t_2,t_3) = \phi_{e_3ge_1}(t_1+t_2+t_3,t_1+t_2,t_1,0), \tag{A9}$$

$$\varphi_A^{(\mathrm{II})}(t_1,t_2,t_3) = \delta_{e_2e_4}\phi_{e_4fe_1}(t_1,t_1+t_2+t_3,t_1+t_2,0), \tag{A10}$$

$$+ (1-\delta_{e_2e_4})\bar\phi_{fe_4e_4e_1}(t_3,t_2,t_1), \tag{A11}$$

with the correlation-induced functions

$$\phi_{cba}(\tau_1,\tau_2,\tau_3,\tau_4) = -g_{cc}(\tau_{43}) - g_{bb}(\tau_{32}) - g_{aa}(\tau_{21}) - g_{cb}(\tau_{42})$$

$$+ g_{cb}(\tau_{43}) + g_{cb}(\tau_{32}) - g_{ca}(\tau_{41}) + g_{ca}(\tau_{42})$$

$$+ g_{ca}(\tau_{31}) - g_{ca}(\tau_{32}) - g_{ba}(\tau_{31}) + g_{ba}(\tau_{32})$$

$$+ g_{ba}(\tau_{21}), \tag{A12}$$

$$\bar\phi_{cbe'e}(t_1,t_2,t_3) = -g_{ee}(t_1) - g_{bb}(t_3) - g_{cc}^*(t_3) - g_{be}(t_1+t_2+t_3)$$

$$+ g_{be}(t_1+t_2) + g_{be}(t_2+t_3) + g_{ce}(t_1+t_2+t_3)$$

$$- g_{ce}(t_1+t_2) - g_{be}(t_2+t_3) + g_{cb}(t_3) + g_{bc}^*(t_3)$$

$$+ g_{ce}(t_2) - g_{be}(t_2) + 2i\,\mathrm{Im}[g_{ce'}(t_2+t_3)$$

$$- g_{ce'}(t_2) - g_{ce'}(t_3) - g_{be'}(t_2+t_3) + g_{be'}(t_2)$$

$$+ g_{be'}(t_3)]. \tag{A13}$$

The linear and third order response functions can now be calculated using Eqs. (11)–(18) with the spectral broadening correlation functions. The 2D signals calculated from the response functions are therefore sensitive to correlations between various transition energy fluctuations through the fluctuation-induced line-shape functions φ which mix all three time intervals.

2. Redfield equations for quantum exciton transport

The density matrix propagator $\mathcal{G}$ in Eqs. (13)–(18) describes free-field density matrix dynamics in the singly excited manifold due to fluctuations of interband couplings. Various levels of theory have been developed to describe system excited state dynamics with the fluctuations. Using the second order perturbation theory within the Markovian approximation, the Green's function satisfies the Redfield equation

$$\frac{d}{dt}\mathcal{G}_{e_4e_3,e_2e_1} = -i\delta_{e_4e_2}\delta_{e_3e_1}\omega_{e_2e_1}\mathcal{G}_{e_2e_1,e_2e_1}$$

$$+ \sum_{e''e'} K_{e_4e_3,e''e'}^{(R)}\mathcal{G}_{e''e',e_2e_1}. \tag{A14}$$

Here $K^{(R)}$ is the Redfield relaxation superoperator. This type of equation may lead to nonphysical, negative, or larger than one exciton probabilities for specific choices of $K^{(R)}$. We therefore use the secular approximation. It decouples the density matrix populations and coherences. In the secular approximation we have

$$K_{e_4e_3,e_2e_1}^{(R)} = (1-\delta_{e_4e_3})\delta_{e_4e_2}\delta_{e_3e_1}\gamma_{e_4e_3} + \delta_{e_4e_3}\delta_{e_2e_1}K_{e_4e_2}. \tag{A15}$$

In our simulations we use the Markovian approximation for the off-diagonal fluctuations. All diagonal fluctuations are

included into the spectral broadening functions. Only lifetime broadenings are then included in the dephasing parameter γ. It gives $\gamma_{ab} = (K_{aa} + K_{bb})/2$. While the relaxation parameters can be calculated using a microscopic bath model of the off-diagonal Hamiltonian fluctuations,[30] we have fitted the rate matrix directly for our phenomenological model.

[1] X. Hu and K. Schulten, Phys. Today **50**, 28 (1997).
[2] V. Sundström, Prog. Quantum Electron. **24**, 187 (2000).
[3] G. Scheibe, Angew. Chem. **49**, 563 (1936).
[4] E. E. Jelley, Nature (London) **138**, 1009 (1936).
[5] A. S. Davydov, *Theory of Molecular Excitons* (Plenum, New York, 1971).
[6] T. Kobayashi, *J-Aggregates* (World Scientific, Singapore, 1996).
[7] E. W. Knapp, P. O. J. Scherer, and S. F. Fischer, Chem. Phys. Lett. **111**, 481 (1984).
[8] H. Fidder, J. Knoester, and D. A. Wiersma, J. Chem. Phys. **95**, 7880 (1991).
[9] T. Meier, V. Chernyak, and S. Mukamel, J. Chem. Phys. **107**, 8759 (1997).
[10] M. Wubs and J. Knoester, Chem. Phys. Lett. **284**, 63 (1998).
[11] H. Fidder, J. Knoester, and D. A. Wiersma, J. Chem. Phys. **98**, 6564 (1993).
[12] V. Sundström, T. Pullerits, and R. van Grondelle, J. Phys. Chem. B **103**, 2327 (1999).
[13] H. Fidder, J. Terpstra, and D. A. Wiersma, J. Chem. Phys. **94**, 6895 (1991).
[14] J. M. Lehn, Science **295**, 2400 (2002).
[15] G. M. Whitesides, J. P. Mathias, and C. T. Seto, Science **254**, 1312 (1991).
[16] A. Pawlik, A. Ouart, S. Kirstein, H.-W. Abraham, and S. Daehne, Eur. J. Org. Chem. **2006**, 3065 (2003).
[17] H. von Berlepsch, C. Böttcher, A. Ouart, C. Burger, S. Dähne, and S. Kirstein, J. Phys. Chem. B **104**, 5255 (2000).
[18] J. Knoester, Int. J. Photoenergy **2006**, 61364 (2006).
[19] L. A. Staehelin, J. R. Golecki, and G. Drewsa, Biochim. Biophys. Acta-Bioenerg. **589**, 30 (1980).
[20] A. R. Holzwarth, K. Griebenow, and K. Schaffner, J. Photochem. Photobiol., A **65**, 61 (1992).
[21] V. I. Prokhorenko, D. B. Steensgaard, and A. R. Holzwarth, Biophys. J. **79**, 2105 (2000).
[22] V. Chernyak and S. Mukamel, J. Chem. Phys. **105**, 4565 (1996).
[23] W. M. Zhang, T. Meier, V. Chernyak, and S. Mukamel, J. Chem. Phys. **108**, 7763 (1998).
[24] M. Yang and G. R. Fleming, J. Chem. Phys. **110**, 2983 (1999).
[25] M. Chachisvilis, T. Pullerits, M. R. Jones, C. N. Hunter, and V. Sundström, Chem. Phys. Lett. **224**, 345 (1994).
[26] T. Joo, Y. Jia, J.-Y. Yu, D. M. Jonas, and G. R. Fleming, J. Chem. Phys. **100**, 2399 (1996).
[27] L. D. Book, A. E. Ostafin, N. Ponomarenko, J. R. Norris, and N. F. Scherer, J. Phys. Chem. B **104**, 8295 (2000).
[28] S. Mukamel, Annu. Rev. Phys. Chem. **51**, 691 (2000).
[29] D. M. Jonas, Annu. Rev. Phys. Chem. **54**, 425 (2003).
[30] D. Abramavicius, B. Palmieri, D. V. Voronine, F. Šanda, and S. Mukamel, Chem. Rev. (Washington, D.C.) **109**, 2350 (2009).
[31] S. Mukamel, D. Abramavicius, Y. Lijun, W. Zhuang, I. V. Schweigert, and D. V. Voronine, Acc. Chem. Res. **42**, 553 (2009).
[32] T. Brixner, J. Stenger, H. M. Vaswani, M. Cho, R. E. Blankenship, and G. R. Fleming, Nature (London) **434**, 625 (2005).
[33] E. L. Read, G. S. Engel, T. R. Calhoun, T. Mancal, T. K. Ahn, R. E. Blankenship, and G. R. Fleming, Proc. Natl. Acad. Sci. U.S.A. **104**, 14203 (2007).
[34] G. S. Engel, T. R. Calhoun, E. L. Read, T.-K. Ahn, T. Mancal, Y.-C. Cheng, R. E. Blankenship, and G. R. Fleming, Nature (London) **446**, 782 (2007).
[35] 1,1′-dioctyl-3,3′-(3-carboxypropyl)-5,5′6, 6′-tetrachlorobenzimidacarbocyanine.
[36] S. Kirstein, H. von Berlepsch, C. Böttcher, C. Burger, A. Ouart, G. Reck, and S. Dähne, ChemPhysChem **1**, 146 (2000).
[37] C. Didraga, J. A. Klugkist, and J. Knoester, J. Phys. Chem. B **106**, 11474 (2002).
[38] C. Didraga and J. Knoester, J. Chem. Phys. **121**, 10687 (2004).
[39] C. Didraga, V. A. Malyshev, and J. Knoester, J. Phys. Chem. B **110**, 18818 (2006).
[40] A. Pugzlys, P. R. Hania, R. Augulis, K. Duppen, and P. H. M. van Loosdrecht, Int. J. Photoenergy **2006**, 29623 (2006).
[41] V. I. Prokhorenko, D. B. Steensgaard, and A. R. Holzwarth, Biophys. J. **85**, 3173 (2003).
[42] A. Pugzlys, R. Augulis, P. H. M. van Loosdrecht, C. Didraga, V. A. Malyshev, and J. Knoester, J. Phys. Chem. B **110**, 20268 (2006).
[43] W. P. de Boeij, M. S. Pshenichnikov, and D. A. Wiersma, J. Phys. Chem. **100**, 11806 (1996).
[44] L. D. Book and N. F. Scherer, J. Chem. Phys. **111**, 792 (1999).
[45] M. L. Cowan, J. P. Ogilvie, and R. J. D. Miller, Chem. Phys. Lett. **386**, 184 (2004).
[46] Y. Tanimura and S. Mukamel, J. Chem. Phys. **99**, 9496 (1993).
[47] M. C. Asplund, M. T. Zanni, and R. M. Hochstrasser, Proc. Natl. Acad. Sci. U.S.A. **97**, 8219 (2000).
[48] J. D. Hybl, A. W. Albrecht, S. M. Gallagher Faeder, and D. M. Jonas, Chem. Phys. Lett. **297**, 307 (1998).
[49] G. D. Goodno, G. Dadusc, and R. J. D. Miller, J. Opt. Soc. Am. B **15**, 1791 (1998).
[50] L. Lepetit and M. Joffre, Opt. Lett. **21**, 564 (1996).
[51] J. D. Hybl, A. A. Ferro, and D. M. Jonas, J. Chem. Phys. **115**, 6606 (2001).
[52] T. Brixner, I. V. Stiopkin, and G. R. Fleming, Opt. Lett. **29**, 884 (2004).
[53] S. Mukamel, *Principles of Nonlinear Optical Spectroscopy* (Oxford University Press, New York, 1995).
[54] J. Piel, E. Riedle, L. Gundlach, R. Ernstorfer, and R. Eichberger, Opt. Lett. **31**, 1289 (2006).
[55] P. Baum and E. Riedle, J. Opt. Soc. Am. B **22**, 1875 (2005).
[56] T. Brixner, T. Mancal, I. V. Stiopkin, and G. R. Fleming, J. Chem. Phys. **121**, 4221 (2004).
[57] A. Moran, J. Maddox, J. Hong, J. Kim, R. Nome, G. Bazan, S. Mukamel, and N. Scherer, J. Chem. Phys. **124**, 194904 (2006).
[58] M. Khalil, N. Demirdöven, and A. Tokmakoff, Phys. Rev. Lett. **90**, 047401 (2003).
[59] M. Khalil, N. Demirdöven, and A. Tokmakoff, J. Phys. Chem. A **107**, 5258 (2003).
[60] S. T. Roberts, J. J. Loparo, and A. Tokmakoff, J. Chem. Phys. **125**, 084502 (2006).
[61] H. von Berlepsch, C. Böttcher, A. Ouart, M. Regenbrecht, S. Akari, U. Keiderling, H. Schnablegger, S. Dähne, and S. Kirstein, Langmuir **16**, 5908 (2000).
[62] M. J. Tauber, R. A. Mathies, X. Chen, and S. E. Bradforth, Rev. Sci. Instrum. **74**, 4958 (2003).
[63] S. Laimgruber, H. Schachenmayr, B. Schmidt, W. Zinth, and P. Gilch, Appl. Phys. B: Lasers Opt. **85**, 557 (2006).
[64] H. von Berlepsch, S. Kirstein, R. Hania, C. Didraga, A. Pugzlys, and C. Böttcher, J. Phys. Chem. B **107**, 14176 (2003).
[65] D. M. Jonas, Science **300**, 1515 (2003).
[66] R. M. Hochstrasser, Nature (London) **434**, 570 (2005).
[67] M. Cho, T. Brixner, I. Stiopkin, H. Vaswani, and G. R. Fleming, J. Chin. Chem. Soc. (Taipei) **53**, 15 (2006).
[68] J. Sperling, F. Milota, A. Tortschanoff, C. Warmuth, B. Mollay, H. Bässler, and H. F. Kauffmann, J. Chem. Phys. **117**, 10877 (2002).
[69] F. Milota, J. Sperling, A. Nemeth, and H. F. Kauffmann, Chem. Phys. **357**, 45 (2009).
[70] I. Stiopkin, T. Brixner, M. Yang, and G. R. Fleming, J. Phys. Chem. B **110**, 20032 (2006).
[71] S. M. Gallagher Faeder and D. M. Jonas, Phys. Rev. A **62**, 033820 (2000).
[72] N.-H. Ge, M. T. Zanni, and R. M. Hochstrasser, J. Phys. Chem. A **106**, 962 (2002).
[73] E. L. Read, G. S. Schlau-Cohen, G. S. Engel, J. Wen, R. E. Blankenship, and G. R. Fleming, Biophys. J. **95**, 847 (2008).
[74] S. Mukamel and D. Abramavicius, Chem. Rev. (Washington, D.C.) **104**, 2073 (2004).
[75] D. Abramavicius, L. Valkunas, and S. Mukamel, EPL **80**, 17005 (2007).
[76] R. S. Mullikan and W. Person, *Molecular Complexes* (Wiley-Interscience, New York, 1969).
[77] V. Chernyak, W. M. Zhang, and S. Mukamel, J. Chem. Phys. **109**, 9587 (1998).
[78] A. Nemeth, F. Milota, J. Sperling, D. Abramavicius, S. Mukamel, and H. F. Kauffmann, Chem. Phys. Lett. **469**, 130 (2009).

[79] A. V. Malyshev, V. A. Malyshev, and J. Knoester, Phys. Rev. Lett. **98**, 087401 (2007).
[80] C. N. Borca, T. Zhang, X. Li, and S. T. Cundiff, Chem. Phys. Lett. **416**, 311 (2005).
[81] P. Hamm, M. Lim, W. F. de Grado, and R. Hochstrasser, Proc. Natl. Acad. Sci. U.S.A. **96**, 2036 (1999).

[82] A. Tortschanoff and S. Mukamel, J. Phys. Chem. A **106**, 7521 (2002).
[83] S.-H. Shim and M. T. Zanni, Phys. Chem. Chem. Phys. **11**, 748 (2009).
[84] T. Zhang, I. Kuznetsova, T. Meier, X. Li, R. P. Mirin, P. Thomas, and S. T. Cundiff, Proc. Natl. Acad. Sci. U.S.A. **104**, 14227 (2007).
[85] D. V. Voronine, D. Abramavicius, and S. Mukamel, J. Chem. Phys. **126**, 044508 (2007).